Pattern dynamics and filamentation of femtosecond terawatt laser pulses in air including the higher-order Kerr effects

T. W. Huang,[1] C. T. Zhou,[1,2,3,*] and X. T. He[1,2]

[1]*HEDPS, Center for Applied Physics and Technology, Peking University, Beijing 100871, People's Republic of China*
[2]*Institute of Applied Physics and Computational Mathematics, Beijing 100094, People's Republic of China*
[3]*Science College, National University of Defense Technology, Changsha 410073, People's Republic of China*

Plasma defocusing and higher-order Kerr effects on multiple filamentation and pattern formation of ultrashort laser pulse propagation in air are investigated. Linear analyses and numerical results show that these two saturable nonlinear effects can destroy the coherent evolution of the laser field, and small-scale spatial turbulent structures rapidly appear. For the two-dimensional case, numerical simulations show that blow-up-like solutions, spatial chaos, and pseudorecurrence can appear at higher laser intensities if only plasma defocusing is included. These complex patterns result from the stochastic evolution of the higher- or shorter-wavelength modes of the laser light spectrum. From the viewpoint of nonlinear dynamics, filamentation can be attributed to the modulational instability of these spatial incoherent localized structures. Furthermore, filament patterns associated with multiphoton ionization of the air molecules with and without higher-order Kerr effects are compared.

I. INTRODUCTION

In recent years, considerable interest in the self-guided propagation of femtosecond terawatt laser pulses in air has been stimulated because of the many potential applications [1–14] such as in lighting discharge control, lidar remote sensing, generation of few-cycle light bullets, and so on. The propagation of ultrashort laser pulses in air is also rich in fundamental nonlinear physics [12–20], including generation of white light, third-order harmonic, terahertz radiation, and conical emission. It is commonly believed that dynamic equilibrium between Kerr compression and plasma diffraction allows femtosecond terawatt laser pulses to self-channel and propagate over a long distance in air. The second-order Kerr self-focusing effect arising from the third-order susceptibility can induce a positive nonlinear refractive index of the air. In principle, for input laser beam having a power above the threshold power (P_{cr}) for self-focusing in air, one can expect that the beam first undergoes a compression process in the diffraction plane and narrower beams can be generated by self-induced waveguiding. However, there is an upper limit to the optical intensity of the light beams. The limit is due to ionization of air molecules when the laser intensity becomes larger than a few tens of TW/cm^2. In a parameter range with the input laser intensity less than 10^{14} W/cm^2, the optically induced ionization can be modeled within the framework of lowest-order perturbation theory and multiphoton ionization processes would be dominant [21], where multiple photons are absorbed by the air molecules and an electron plasma can be generated. The resulting electron plasma has a diverging effect on the light pulse, since it has a negative contribution to the refractive index of the air. Dynamic balance between the Kerr self-focusing and the diffraction of the plasma results in filamentation of the light beam that can last for a distance much longer than the Rayleigh length [10,11]. The first experimental observation of long-distance self-guided laser propagation in

air was shown in the mid-1990s, where a plasma channel as long as 20 m was observed [12]. Later, it was shown that an intense femtosecond pulse laser beam launched vertically into the sky can generate white light at a distance of 10 km [13,14]. The optical intensities inside a filament can reach a few tens of TW/cm^2. Such laser-induced supercontinuum light can be useful for detecting pollutants in the atmosphere [13].

There exist many theories, simulations, and experiments on self-channeling of intense femtosecond laser pulses in air [1–62]. The critical power for self-focusing is one of the key parameters in laser filamentation in air. As is well known, if the pulse power is less than a few critical powers, only one filament is formed. At much higher powers, a single laser pulse can form several filaments—a process known as multiple filamentation. The generation of multiple filaments is usually explained in terms of modulation instability of the laser beam [22] and an optically turbulent light guide model [23]. It has been proposed that the multiple filaments can be regarded as the propagation of a group of interacting light filaments [24]. In the proposed models, plasma diffraction due to multiphoton ionization of the air molecules is invoked for the formation of the self-guided light channel. However, for balancing the second-order nonlinear Kerr focusing, the saturation of the Kerr effect or the so-called higher-order Kerr effects (HOKE) have also been suggested to play an important role [25–46]. It is well known that the high-order saturation effect in a nonlinear Schrödinger equation (NLSE) can lead to spatialtemporal chaos and complicated patterns of light waves propagating in a medium [47]. Recently, some experiments have measured the coefficients of the higher-order terms up to n_8 in nitrogen and oxygen and n_{10} for argon [25]. The data showed that the different-ordered nonlinear Kerr terms in the refractive index have different signs, and the higher-order Kerr effects can provide a defocusing effect. Filaments can then be formed when the nonlinear refractive index change signs from positive to negative with the increase of laser intensity [26–28]. However, it is mentioned that subsequent experimental results do not support such a higher-order Kerr

*zcangtao@iapcm.ac.cn

model [29–33]. Recently, some attention has been paid to these two mechanisms of laser filamentation in air [25–46]. It is found that HOKE can improve the quantitative modeling of laser filamentation with respect to the peak intensity and electron density in the laser filaments [34,35]. However, these results cannot be reproduced by other experiments and simulations [29–33,36–38]. On the other hand, the HOKE model cannot fully produce the experimental conical emissions although the classical model can [39]. A more detailed understanding of laser filamentation in air is, therefore, still needed.

Both plasma diffraction and HOKE can balance nonlinear Kerr focusing in laser propagation in air. It should be noted that these two models balance Kerr focusing for different parameter ranges. For instance, for infrared laser pulses with duration of about 100 fs, the nonlinear refractive index saturates and goes to negative at a lower intensity in HOKE model than that in classical case [25,34,35,48], where the plasma defocusing is considered a saturating nonlinearity. For such generalized saturable NLSEs, our previous investigations [47] illustrated that spatial chaos and complicated patters can be formed due to high-order saturable effects. In particular, it is found that the nonlinear propagation of ultrashort laser pulses in air can become incoherent and chaotic by invoking a fifth-order susceptibility [49]. We note that filamentation instability, solitary waves, and spatial chaotic patterns are the result of nonlinear development of the modulational instability for unstable wave modes [63–66]. It is, therefore, of interest to investigate problems of pattern dynamics and filamentation of femtosecond terawatt laser pulses in air including higher-order Kerr nonlinearity and plasma diffraction. Such an investigation may throw a new light onto the better understanding of the filamentation process in air.

In the present paper, we theoretically and numerically investigate spatial chaos and multiple filamentation of ultrashort laser pulses in air by taking into account multiphoton ionization of the air molecules without and with higher-order Kerr nonlinear effects. The numerical simulations are carried out based on a NLSE including HOKE [25] and a high-order plasma saturation term that describes the multiphoton ionization of the air molecules [48]. We aim to provide a deeper understanding of the influence of the higher-order nonlinear effects (including both HOKE and plasma saturable effects) on the nonlinear propagation of ultrashort laser pulses in air. In particular, we hope to establish a link between nonlinear dynamical theory and filamentation processes. The paper is organized as follows. In Sec. II, we give a brief introduction of the reduced physical model describing the ultrashort laser pulses propagating in air, and qualitative analysis of the physical model is also given. The spatial chaos and pattern dynamics in one and two dimensions are discussed in Sec. III and Sec. IV, respectively. The effect of HOKE and plasma diffraction on multiple filamentation of femtosecond terawatt laser pulses in air is investigated in Sec. V. A conclusion is given in the last section.

II. PHYSICAL MODEL AND QUALITATIVE ANALYSIS

The generalized NLSE is often considered a universal model describing wave collapse and strong turbulence [66,67].

It has widely been applied in continuum mechanics, nonlinear optics, plasma physics, Bose-Einstein condensates [67], and so on. Recently, a full $3D + 1$ dimensional NLSE model describing a linearly polarized paraxial laser beam propagating in air was developed [50,51]. In this model, the vectorial effects [68] due to tight focusing and nonparaxial propagation of the laser are not considered. Moreover, numerical integration of the full $3D + 1$ dimensional model over long distances is often limited by the computer capacity. If we only focus on the spatial dynamics of the laser pulse, a time-averaged $2D + 1$ dimensional model that can well reproduce the qualitative features of the experimentally observed patterns can be employed [48]. In addition, such a reduced model can provide a reasonable approximation of fluence patterns developed by the full $(3D + 1)$-dimensional model, which makes it be widely used to capture the transverse dynamics of the filamentation phenomenon [48,49,69]. For multiple filamentation problem, such a reduced model can be employed to capture the main characteristics of the multiple-filament patterns. Including HOKE, this model for the evolution of the scalar envelope $E(x,y,z)$ in the frame traveling at the pulse velocity is given by the equation [34,50]

$$\partial_z E = i \frac{1}{2k_0 n_0} \nabla_\perp^2 E + i k_0 \Delta n E - i\gamma |E|^{2K} E, \quad (1)$$

where $\nabla_\perp^2 = \partial_{xx}^2 + \partial_{yy}^2$ is the transverse Laplace operator, $k_0 = 2\pi n_0/\lambda_0$ is the wave number in vacuum, n_0 is the linear index of refraction of the medium, $\lambda_0 (= 800$ nm$)$ is the central wavelength of the laser, $\Delta n = \frac{n_2}{\sqrt{3}}|E|^2 + \frac{n_4}{\sqrt{5}}|E|^4 + \frac{n_6}{\sqrt{7}}|E|^6 + \frac{n_8}{3}|E|^8$ is the nonlinear refractive index of the medium, the scalar envelop $E(x,y,z)$ is defined as $|E|^2 = I$, and I is the incident laser intensity. The last term on the right-hand side of Eq. (1) represents the plasma defocusing effect. Here $\gamma = k_0 \sigma_K \rho_{nt}\sqrt{\pi/(8K)}T/(2n_c)$, where $\sigma_K \approx 2.88 \times 10^{-99}$ s^{-1} cm^{2K}/W^K is the coefficient of multiphoton ionization, K is the number of photons, say $K = 8$ for O$_2$ gas, $\rho_{nt} \approx 5.4 \times 10^{18}$ cm^{-3} is the neutral density, $n_c \approx 1.8 \times 10^{21}$ cm^{-3} is the critical plasma density, and $T \approx t_p/10$ with $t_p = 85$ fs is the half-width of the laser pulse duration. It is noted here that multiphoton absorption (MPA) is not considered in our system in order to obtain a better understanding of the difference between the two different saturable effects, as well for the fact that in the presence of HOKE the MPA does not play an important role [34,42,43] in filamentation. To be more concrete, in most of the simulations we assume the propagation medium is O$_2$ gas. For comparison, in Sec. III we also discuss several simulations for N$_2$. The corresponding experimental parameters [25] are listed in Table I.

The system of Eq. (1) is nondissipative and can be expressed in a dimensionless form as

$$i\partial_z E(\mathbf{x},z) + \nabla_\perp^2 E(\mathbf{x},z) + F(|E|^2)E(\mathbf{x},z) = 0, \quad (2)$$

where $F(|E|^2) = \alpha|E|^2 + \beta(\beta_4|E|^4 + \beta_6|E|^6 + \beta_8|E|^8) - \gamma_K|E|^{2K}$ and $\mathbf{x}$, E, z are normalized by w_0, $\sqrt{P_{cr}/4\pi w_0^2}$, and $4z_f$, respectively. Here $z_f = \pi w_0^2/\lambda_0$ is the Rayleigh length and $P_{cr} \approx 3.77\lambda_0^2/8\pi n_0 n_2$ is the critical power for self-focusing. For the O$_2$ case with $\lambda_0 = 800$ nm, we have $\alpha = 0.544$, $\beta = -1$, $\beta_4 = 6.541 \times 10^{-6}$ /$(w_0/$cm$)^2$, $\beta_6 = -2.4364 \times 10^{-10}$ /$(w_0/$cm$)^4$, $\beta_8 = 4.489 \times 10^{-14}$ /$(w_0/$cm$)^6$,

TABLE I. Indices of the higher-order refraction terms in both N_2 and O_2.

Mediums	$n_2(10^{-19}cm^2/W)$	$n_4(10^{-33}cm^4/W^2)$	$n_6(10^{-46}cm^6/W^3)$	$n_8(10^{-59}cm^8/W^4)$
N_2	1.1	−0.53	1.4	−0.44
O_2	1.6	−5.16	4.75	−2.1

$\gamma_K = 2.7115 \times 10^{-37}/(w_0/cm)^{2K-2}$, and $w_0 = 0.3$ cm is the transverse width of the laser beam. These values will be used in Sec. IV.

We now consider the invariants of our system. Equation (2) can be derived from the Lagrangian density $L = \frac{i}{2}(E^*E_z - EE_z^*) - |\nabla_\perp E|^2 + \frac{1}{2}\alpha|E|^4 + \beta(\frac{1}{3}\beta_4|E|^6 + \frac{1}{4}\beta_6|E|^8 + \frac{1}{5}\beta_8|E|^{10}) - \frac{1}{K+1}\gamma_K|E|^{2K+2}$. According to the Noether's theorem, we can obtain three invariants [66]: the wave power $P = \int |E|^2 d\mathbf{x}$, the momentum $M = \frac{i}{2}\int(E_\mathbf{x}E^* - EE_\mathbf{x}^*)d\mathbf{x}$, and the Hamiltonian

$$H = \int [|\nabla_\perp E|^2 - \frac{1}{2}\alpha|E|^4 - \beta\left(\frac{1}{3}\beta_4|E|^6 + \frac{1}{4}\beta_6|E|^8 \right.$$
$$\left. + \frac{1}{5}\beta_8|E|^{10}\right) + \frac{1}{K+1}\gamma_K|E|^{2K+2}]d\mathbf{x}. \quad (3)$$

From Eq. (3), the Hamiltonian of the system (2) can be separated into two parts: $H = H_0 + H_1$, where $H_0 = \int(|\nabla_\perp E|^2 - \frac{\alpha}{2}|E|^4)d\mathbf{x}$ is the Hamiltonian of cubic NLSE and $H_1 = \int[-\beta(\frac{1}{3}\beta_4|E|^6 + \frac{1}{4}\beta_6|E|^8 + \frac{1}{5}\beta_8|E|^{10}) + \frac{1}{K+1}\gamma_K|E|^{2K+2}]d\mathbf{x}$ is the Hamiltonian perturbation of system (2) induced by HOKE and plasma diffraction.

For Eq. (2), a simple plane-wave solution can be written as $E_s = E_0 e^{iF(E_0^2)z}$. Now we give a qualitative analysis of the dynamic behavior of this homogeneous solution exposed to the modulational instability. Let $\delta E(\mathbf{x},z)$ be a small perturbation from E_s, so $E(\mathbf{x},z) = E_s(z) + \delta E(\mathbf{x},z)$, where $|\delta E| \ll |E_s|$. Linearizing Eq. (2) around E_s, we obtain the equation for the eigenfunction $\delta E(\mathbf{x},z)$,

$$\begin{pmatrix} i\partial_z + \nabla_\perp^2 + \text{Re} & h(z) \\ h^*(z) & -i\partial_z + \nabla_\perp^2 + \text{Re} \end{pmatrix}\begin{pmatrix} \delta E \\ \delta E^* \end{pmatrix} = 0, \quad (4)$$

where $\text{Re} = F(E_0^2) + F'(E_0^2)E_0^2$, $h(z) = F'(E_0^2)E_s^2$, and $F'(u) = \partial_u F$.

Assuming periodic boundary conditions, $\delta E(x,z)$ can be expressed as [70]

(i) a one-dimensional case,

$$\begin{pmatrix} \delta E \\ \delta E^* \end{pmatrix} = \begin{pmatrix} \epsilon e^{i\lambda z} \\ \epsilon^* e^{-i\lambda^* z} \end{pmatrix}\cos(k_x x), \quad (5)$$

(ii) a two-dimensional case,

$$\begin{pmatrix} \delta E \\ \delta E^* \end{pmatrix} = \begin{pmatrix} \epsilon e^{i\lambda z} \\ \epsilon^* e^{-i\lambda^* z} \end{pmatrix}\cos(k_x x)\cos(k_y y), \quad (6)$$

where ϵ and ϵ^* are small parameters and k is the wave number of the perturbation. Inserting Eqs. (5) and (6) into (4), we obtain the eigenvalue

$$\lambda = F(E_0^2) \pm ik\sqrt{2F'(E_0^2)E_0^2 - k^2}, \quad (7)$$

and the linear growth rate $\Gamma = k\sqrt{2F'(E_0^2)E_0^2 - k^2}$ of the modulational instability for $k^2 < 2F'(E_0^2)E_0^2$, where $k = k_x$ for the one-dimensional case and $k = \sqrt{k_x^2 + k_y^2}$ for the two-dimensional case. The wave number of the most unstable mode is then $k_{max} = E_0\sqrt{F'(E_0^2)}$ for the one-dimensional case and $k_{x,max} = k_{y,max} = E_0\sqrt{F'(E_0^2)/2}$ for the two-dimensional case, respectively. Inserting Eqs. (5) and (7) into Eq. (4), we obtain $\frac{\delta E}{\delta E^*}|_{z=0} = \pm i$, which is very important for analyzing the nonlinear behavior of Eq. (2). In order to illustrate
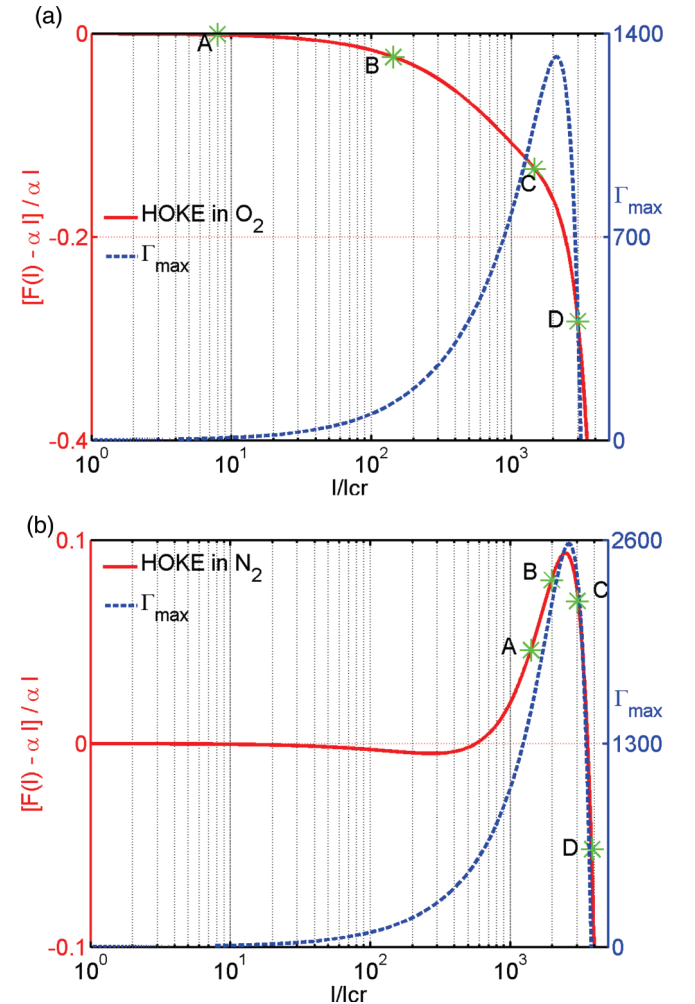

FIG. 1. (Color online) Values of HOKE relative to the KF effect (solid red line) and most unstable growth rate of modulational instability (dashed blue line) at different intensity of input laser (I_0) for the O_2 case (a) and the N_2 case (b). Asterisk symbols in (a) mark the points with I_0 of $8I_{cr}$, $150I_{cr}$, $1500I_{cr}$, $3000I_{cr}$, respectively, and in (b) the asterisk symbols correspond to $1500I_{cr}$, $2000I_{cr}$, $3000I_{cr}$, $3700I_{cr}$, respectively, where $I_{cr} = P_{cr}/4\pi w_0^2 \approx 5.305 \times 10^9 W/cm^2$ for O_2 and $7.717 \times 10^9 W/cm^2$ for N_2.

its importance, we construct the phase space $(|E|, d|E|/dz)$ at $\mathbf{x} = 0$ and assume the initial condition $E(x,0) = E_0 + \epsilon e^{i\theta}\cos(k_x x)$ for the one-dimensional case and $E(x,y,0) = E_0 + \epsilon e^{i\theta}\cos(k_x x)\cos(k_y y)$ for the two-dimensional case, where ϵ is a small real parameter. Although such a low-dimensional phase space is only a projection of high-dimensional space, it can reasonably describe homoclinic crossing of the one-dimensional cubic integrable NLSE equation (see Fig. 2(b); also see Fig. 3(a) in Ref. [70]). Obviously, the unstable manifolds of the hyperbolic fixed point $(E_0, 0)$ in this phase space correspond to $\theta = 45°$ and $225°$, and the stable manifolds correspond to $\theta = 135°$ and $315°$. To obtain both stable and unstable manifolds (corresponding to a homoclinic orbit (HMO) [49,63–65,71]) for the hyperbolic fixed point $(E_0, 0)$, one can directly solve Eq. (2) [47,49,70] by choosing $\pm h$ (h is the numerical step).

III. SPATIAL CHAOS IN ONE-DIMENSIONAL TRANSVERSE SPACE

We now turn to numerical simulations of the nonlinear system (2). First, we would discuss the influence of HOKE on the pattern dynamics of ultrashort laser pulses in air for the one-dimensional case. The two-dimensional problem will be

TABLE II. Coefficients of the Kerr refraction terms in Eq. (8).

Mediums	α	$\beta_4(10^{-4})$	$\beta_6(10^{-8})$	$\beta_8(10^{-11})$
N_2	3.77/4	0.3504	−7.1431	1.7324
O_2	3.77/4	1.6251	−7.9583	1.8472

discussed in the next section. When only HOKE is considered, Eq. (2) in the one-dimensional case can be written as

$$i\partial_z E(x,z) + \partial_x^2 E(x,z) + F(|E|^2)E(x,z) = 0, \qquad (8)$$

where $F(|E|^2) = \alpha|E|^2 - (\beta_4|E|^4 + \beta_6|E|^6 + \beta_8|E|^8)$. In this case, we consider the different propagation mediums such as N_2 and O_2. In particular, for N_2, HOKE has a positive contribution to the refractive index of air when the intensity of the laser pulse is in the region $4.49 \times 10^{12} < I_0$ (W/cm^2) $< 2.74 \times 10^{13}$, which could induce a quite different behavior on the pattern dynamics compared with the case of O_2 [69]. The coefficients in $F(|E|^2)$ for both N_2 and O_2 are listed in Table II, where $w_0 = 0.3$ cm and $\lambda_0 = 800$ nm are taken.

According to the analysis in Sec. II, we have given a reasonable initial condition and a suitable phase space to analyze nonlinear dynamic properties of Eq. (8). In our numerical simulations, we assume different input laser
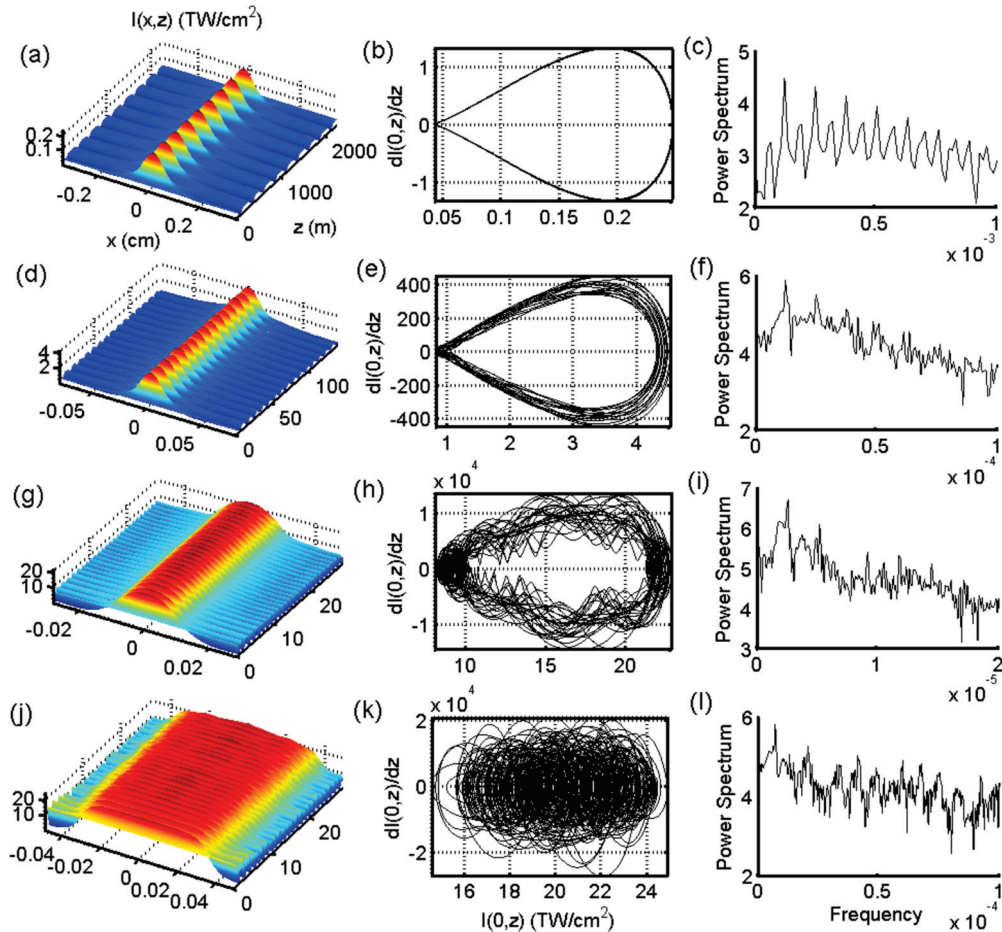

FIG. 2. (Color online) Pattern structures of laser fields [(a), (d), (g), and (j)], phase space computed from the series $(|E(0,z)| \sim z)$ [(b), (e), (h), and (k)] and the corresponding power spectrum (arbitrary unit) [(c), (f), (i), and (l)] with I_0, respectively, of $8I_{cr}$ [(a)–(c)], $150I_{cr}$ [(d)–(f)], $1500I_{cr}$ [(g)–(i)], and $3000I_{cr}$ [(j)–(l)] for the O_2 case, corresponding to the points in Fig. 1(a).

intensities (different E_0), with a perturbation level of $0.01E_0$ and initial phase $\theta = 45°$. We also consider the most unstable mode with $k = k_{max}$. In addition, the standard spectral method has been employed for transverse space (x direction) integration with a periodic length $L = 2\pi/k_{max}$ and the fourth-order Runge-Kutta method with variable step for propagation along the z direction.

If only the Kerr focusing (KF) is considered, the Hamiltonian of the system (8) becomes $H = H_0$. Equation (8) reduces to the well-known cubic NLSE that is fully integrable in the one-dimension case due to the existence of a Lax pair [72]. For the cubic NLSE, a class of periodic solutions and solitons can be obtained by use of an inverse scattering transform, and the solitons developed by modulational instabilities keep their spatially coherent structures and temporally periodic evolutions [70–73]. In terms of our dynamical system (8), HOKE acts as a Hamiltonian perturbation H_1 to H_0. In Fig. 1, we give the values of HOKE relative to the KF term and most unstable growth rate $\Gamma_{max} = F'(E_0^2)E_0^2$ at different I_0 for both the N_2 and O_2 cases. In the context of the specific coefficients provided in the experiments [25], it is shown that for O_2 HOKE can always provide a negative contribution to the refractive index; however, for N_2, HOKE cannot. Figure 1(b) shows that when I_0 lies in the region $4.49 \times 10^{12} < I_0$ (W/cm^2)

$< 2.74 \times 10^{13}$, HOKE becomes a positive perturbation due to rapid increase of the high-order focusing term $\beta_6|E|^6$ in HOKE, and, correspondingly, Γ_{max} increases quickly. In addition, the weaker defocusing term in HOKE for N_2 leads to a much larger Γ_{max} than that for O_2, which would result in a quite different behavior of the evolutions of laser field in the two mediums.

Figure 2 shows the solutions of Eq. (8) at different I_0 for O_2 case. When I_0 is small enough [see point A in Fig. 1(a)], HOKE relative to the KF effect is very small and the perturbation H_1 from HOKE can be neglected. As illustrated above, laser propagation obeys an integrable cubic NLSE with only the KF term. A typical periodic recurrent solution is obtained in Fig. 2(a): spatially coherent pattern structures appear and propagate with an invariable velocity. In a sense, the periodic motion consists of two stages as predicted by Benjamin and Fair [74]. The unstable modulation of the uniform solution would first grow at an exponential rate, but eventually the solution would demodulate and return to a near-uniform state. The corresponding phase-space trajectory is a HMO or the Kolmogorov-Arnold-Moser (KAM) tori, where the unstable manifold smoothly joins with the stable manifold at the saddle point $(I_0,0)$ [70]. Such a soliton-like structure has also been obtained for relativistically intense
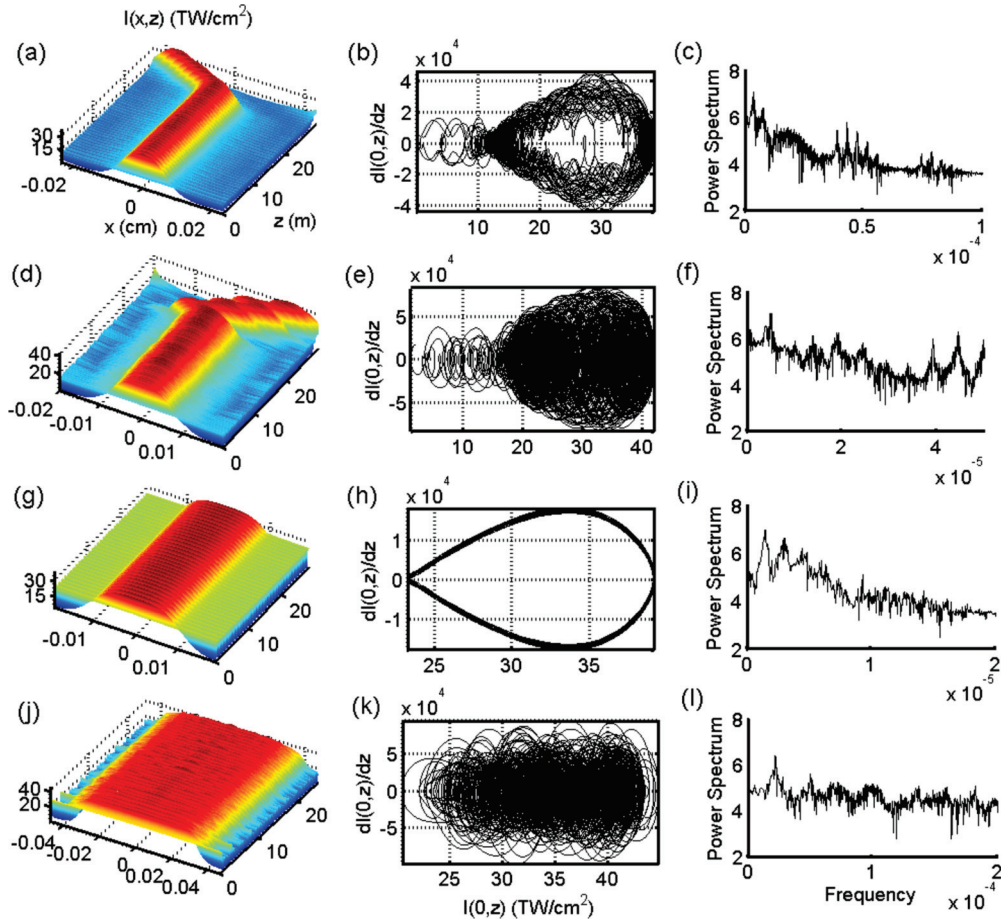

FIG. 3. (Color online) Pattern structures of laser fields [(a), (d), (g), and (j)], phase space computed from the series ($|E(0,z)| \sim z$) [(b), (e), (h), and (k)] and corresponding power spectrum (arbitrary unit) [(c), (f), (i), and (l)] with I_0, respectively, of $1500I_{cr}$ [(a)–(c)], $2000I_{cr}$ [(d)–(f)], $3000I_{cr}$ [(g)–(i)], and $3700I_{cr}$ [(j)–(l)] for the N_2 case, corresponding to the points in Fig. 1(b).
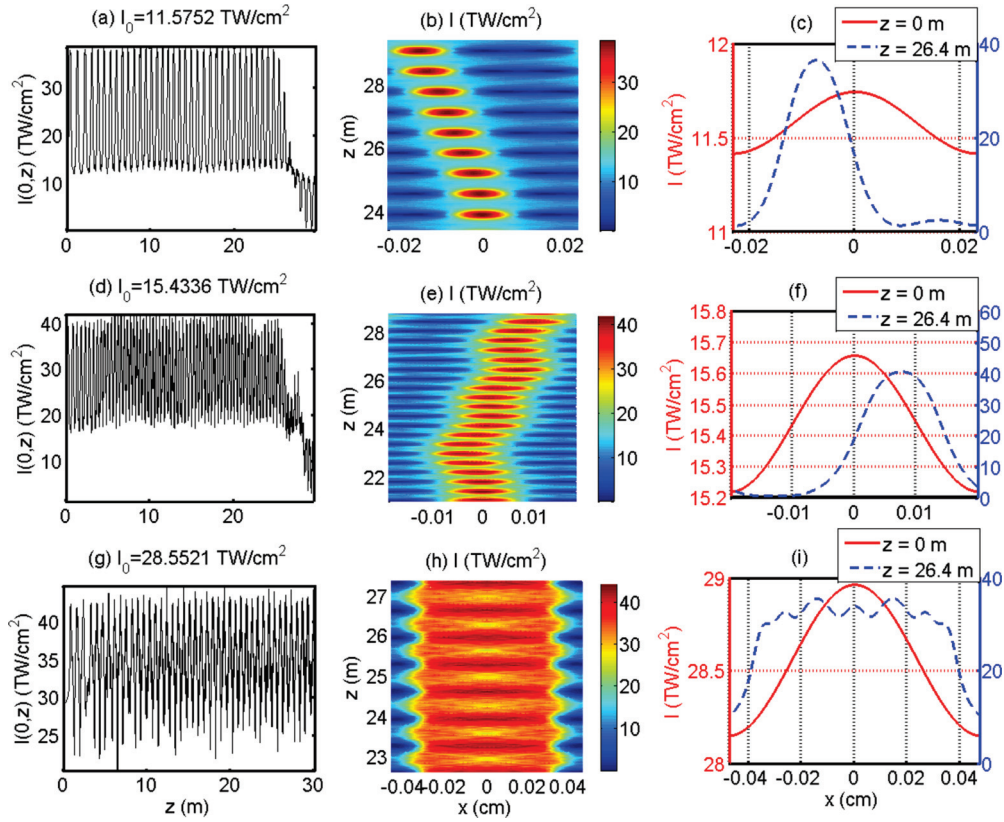
FIG. 4. (Color online) Comparison of the two different complicated spatial patterns with I_0 respectively of $1500I_{cr}$ [(a)–(c)], $2000I_{cr}$ [(d)–(f)], and $3700I_{cr}$ [(g)–(i)] for N_2 case. [(a), (d), and (g)] Evolutions of laser field at $x = 0$. [(b), (e), and (h)] The contours of laser intensity $I(x,z)$. [(c), (f), and (i)] The profile of laser intensity at $z = 0$ (solid red line) and 26.4 m (dashed blue line).

laser in underdense plasmas [75,76], where the relativistic effect and the ponderomotive force dominate the propagation. For $I_0 = 150I_{cr}$ [see point B in Fig. 1(a)], the first defocusing term in HOKE ($\beta_4|E|^4$) cannot be neglected and HOKE begins to play an important role. As a result, the laser fields exhibit a weak chaotic behavior [63,64]: The pattern structure does not recur within the finite distance and KAM tori in phase space become much thicker, as shown in Fig. 2(e). In a sense, this kind of solution is also called a quasiperiodic solution [70]. The corresponding power spectra shown in Fig. 2(f) indicate that many subharmonics appear compared with that in Fig. 2(c).

When laser intensity increases to $1500I_{cr}$ (or 7.96×10^{12} W/cm^2) [see point C in Fig. 1(a)], the second focusing term in HOKE ($\beta_6|E|^6$) becomes a large perturbation but is dominated by the stronger defocusing effect in HOKE. At this point, HOKE can completely break down the KAM tori in phase space and the noiselike power spectra shown in Fig. 2(i) demonstrate that strong chaos occurs. However, for N_2, as shown in Fig. 1(b), when the laser intensity I_0 increases to 4.49×10^{12} W/cm^2, the second focusing term in HOKE ($\beta_6|E|^6$) dominates $\beta_4|E|^4$ and becomes an important mechanism. As a result, the HOKE turns from a negative perturbation to a positive perturbation, leading to the sharp increase of the maximum growth rate of modulational instability and quickly breakdown of the system. Complicated pattern structures with a continuous phase shift and off-axis evolution are observed for $4.49 \times 10^{12} < I_0$ (W/cm^2) $< 1.91 \times 10^{13}$, in which the focusing term $\beta_6|E|^6$

becomes a large perturbation [69]. Such complex patterns differ substantially from that given in Fig. 2(g). Particularly, for $I_0 = 1500I_{cr}$ ($\approx 1.16 \times 10^{13}$ W/cm^2) [see point A in Fig. 1(b)], the laser intensity $I(x,z)$ experiences a stochastic oscillation at sufficiently far distance and the pattern drifting phenomenon [77] is shown in Fig. 3(a) [also Fig. 4(b)]. For $I_0 = 2000I_{cr}$ ($\approx 1.54 \times 10^{13}$ W/cm^2) [see point B in Fig. 1(b)], more complicated pattern structures with oscillated centroids that differ from the pattern drifting are shown in Fig. 3(d) [also Fig. 4(e)]. It is noted that the found off-axis evolution, as shown in Figs. 4(b) and 4(e), corresponds to the most unstable stage of the system. When the modulational instability is strong enough (a very large Γ_{max}), the laser fields with quite small noise can easily develop into such complex structures. In addition, the off-axis propagation of high-intensity laser pulses in underdense plasmas can lead to laser hosing instability [78]. Thus, the off-axis behavior should be a general characteristic of laser pulse propagation in the real medium, where the asymmetric factors of the laser field would be quickly enlarged by the modulational instability. Furthermore, the corresponding phase-space trajectories shown in Figs. 3(b) and 3(e) demonstrate that the KAM tori are completely broken down and irregular HMO crossings gradually appear with the off-axis evolution of the laser field. As we have known, irregular HMO crossings are associated with spatiotemporal chaos [70,71] and pattern competition [77]. Differing from pattern competition that experiences a phase jump from $\theta = 45°$ to $\theta = 225°$, these two complicated patterns shown in
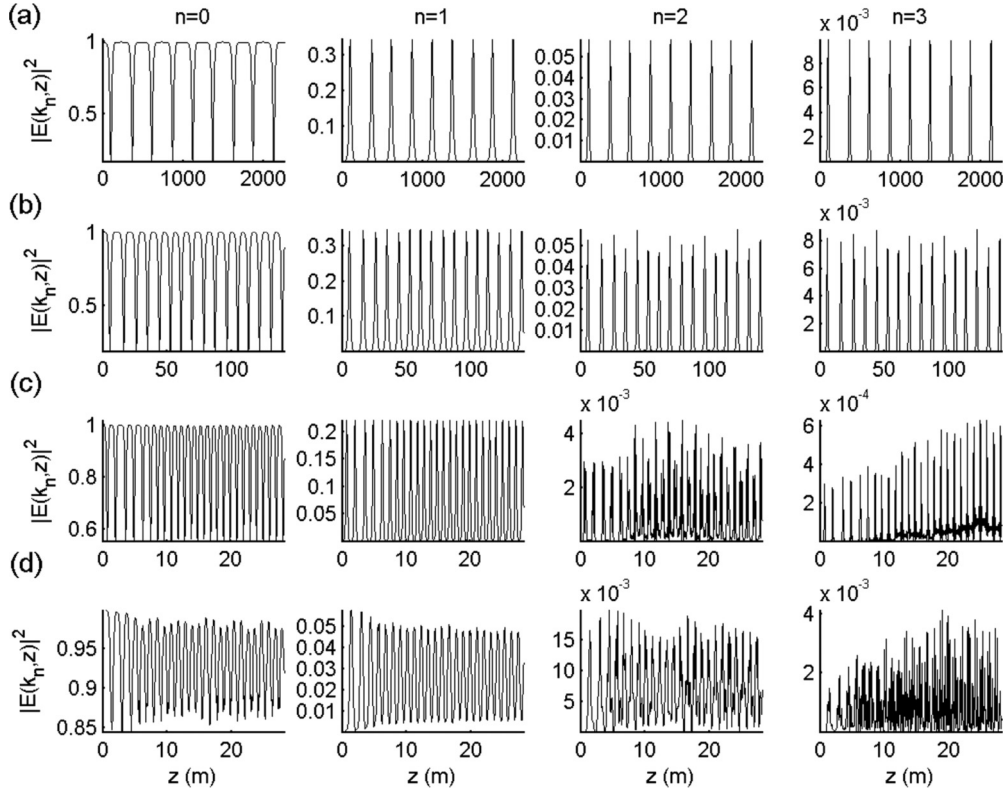
FIG. 5. The energy evolution in the Fourier modes for the O_2 case with I_0, respectively, of $8I_{cr}$ (a), $150I_{cr}$ (b), $1500I_{cr}$ (c), and $3000I_{cr}$ (d) as shown in Fig. 1(a).

Figs. 3(a) and 3(d) experience a continuous phase shift from $\theta = 45°$ to $\theta = 225°$. On the other hand, the trajectories of off-axis evolution are extremely sensitive to the initial laser intensity, which is typical for a chaotic system [63,64], further demonstrating that strong chaos occur in this case.

For the N_2 case, when laser intensity increases further to 2.74×10^{13} W/cm^2, the third defocusing term in HOKE ($\beta_8|E|^8$) dominates the focusing term $\beta_6|E|^6$ and results in another transition for HOKE from a positive perturbation to a negative perturbation again. In addition, the negative HOKE experiences a dramatic increase with the increase of laser intensity [see Fig. 1(b)]. For I_0 (W/cm^2) $> 2.74 \times 10^{13}$, another complicated pattern which differs completely from the ones discussed above is observed. Particularly, for $I_0 \approx 2.86 \times 10^{13}$ W/cm^2 [see point D in Fig. 1(b)], the complicated pattern and relevant stochastic phase-space trajectory are shown in Figs. 3(j) and 3(k). In Fig. 4, we give a comparison between the off-axis patterns and this complicated pattern. It is shown that at the same propagation distance z, the former exhibits off-axis behavior, while the latter first experiences a quick spatial diffraction and then develops into many small-scale spatial structures. Because of the interaction of these small-scale waves, their spatial structures experience a stochastic change with the propagation of laser field, leading to the chaotic behavior of laser field shown in Fig. 4(g). The interaction of different short waves can lead to more complicated spatial structures. It is also important to point out that although the corresponding laser field propagates with a quite complicated oscillation behavior, Fig. 4(h) shows that their patterns are still of on-axis structures. In addition, for $I_0 \approx 2.3 \times 10^{13}$ W/cm^2

[see point C in Fig. 1(b)], Fig. 3(g) shows that the laser propagation experiences a quasiperiodic process. Therefore, our simulations demonstrate that the off-axis pattern [in Figs. 3(a) and 3(d)] can again become the on-axis pattern [in Fig. 3(j)] by a quasiperiodic pattern [as shown in Fig. 3(g)]. Such complicated patterns have also been shown in Fig. 2(j) when laser intensity increases to 1.06×10^{13} W/cm^2. Their corresponding continuous power spectra shown in Fig. 2l and Fig. 3l reveal the chaotic behavior.

In order to analyze the mechanism that leads to these chaotic behaviors, we further investigate the evolution of energy contained in Fourier modes. In Fourier space, the energy of the system (8) can be defined as

$$H = \sum_n H_{K_n} = \sum_n |E_{K_n}|^2, \qquad (9)$$

where the initial energy is in the mode k_{max}. Figure 5 shows the evolution of the energy in the first four Fourier modes corresponding to the solutions shown in Fig. 2. Obviously, a large part of the energy lies in the first and second Fourier modes. For $I_0 = 8I_{cr}$, the evolution of energy in all modes is periodic [see Fig. 5(a)], which is consistent with periodic recurrent patterns shown in Fig. 2(a). For $I_0 = 150I_{cr}$, the quasiperiodic evolution of energy in Fourier modes shown in Fig. 5(b) also agrees with the quasiperiodic solution shown in Fig. 2(d), whereas for $I_0 = 1500I_{cr}$ and $3000I_{cr}$, Figs. 5(c) and 5(d) show that energy in the system would spread from the lowest mode to many higher modes due to HOKE and would not regroup into the original lowest mode. We can also see from Figs. 5(c) and 5(d) that the quasiperiodic evolution
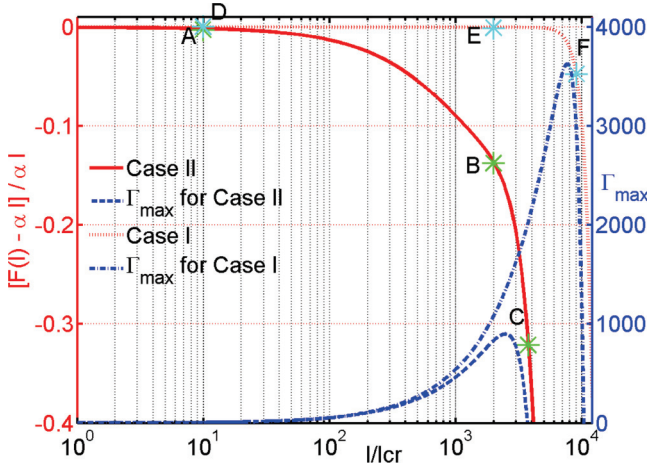
FIG. 6. (Color online) Comparison of the values of nonlinear terms (solid red line for Case II and dotted red line for Case I) and the corresponding most unstable growth rate Γ_{max} of modulational instability (dashed blue line for Case II and dash-dotted blue line for Case I) in two cases, where the asterisk symbols in Case I mark the points with I_0 of $10I_{cr}$, $2000I_{cr}$, $9000I_{cr}$, and in Case II the asterisk symbols correspond to $10I_{cr}$, $2000I_{cr}$, $3600I_{cr}$, respectively. Here, $I_{cr} = P_{cr}/4\pi w_0^2 \approx 5.305 \times 10^9 \text{W/cm}^2$.

of the energy in the first two modes dominates the spatially localized structures being kept. However, the evolution of energy in higher modes clearly exhibits stochastic behavior

due to the strong mode-mode interactions, which would lead to the presence of complicated spatial patterns, as shown in Figs. 2(g) and 2(j).

IV. SPATIOTEMPORAL PATTERNS IN TWO-DIMENSIONAL TRANSVERSE SPACE

In this section, we turn to discussing the dynamic characteristics of the system (2) in two-dimensional transverse space. In this case, both the HOKE and plasma diffraction are considered. As we have known, the filamentation processes in air are mainly investigated in high-dimensional space [58–62]; however, nonlinear properties of ultrashort laser propagating in air, including the spatial chaos and pattern formation, have not been investigated in high-dimensional spaces. For two-dimensional NLSE, the singular focusing solution exists [79–81], pseudorecurrence can also appear when the saturable nonlinear effects are strong enough [82], and even a solitary solution can be produced with an appropriate positive potential [83]. We here investigated the nonlinear pattern dynamics of the system (2) in two-dimensional transverse spaces by taking into account the high-order plasma saturation effect without and with higher-order Kerr nonlinear effects. In the numerical simulation, we employ the same initial condition and numerical method as discussed in Sec. III. The most unstable mode with $k_x = k_{x,max}$ and $k_y = k_{y,max}$ is considered and we assume the medium is O_2.
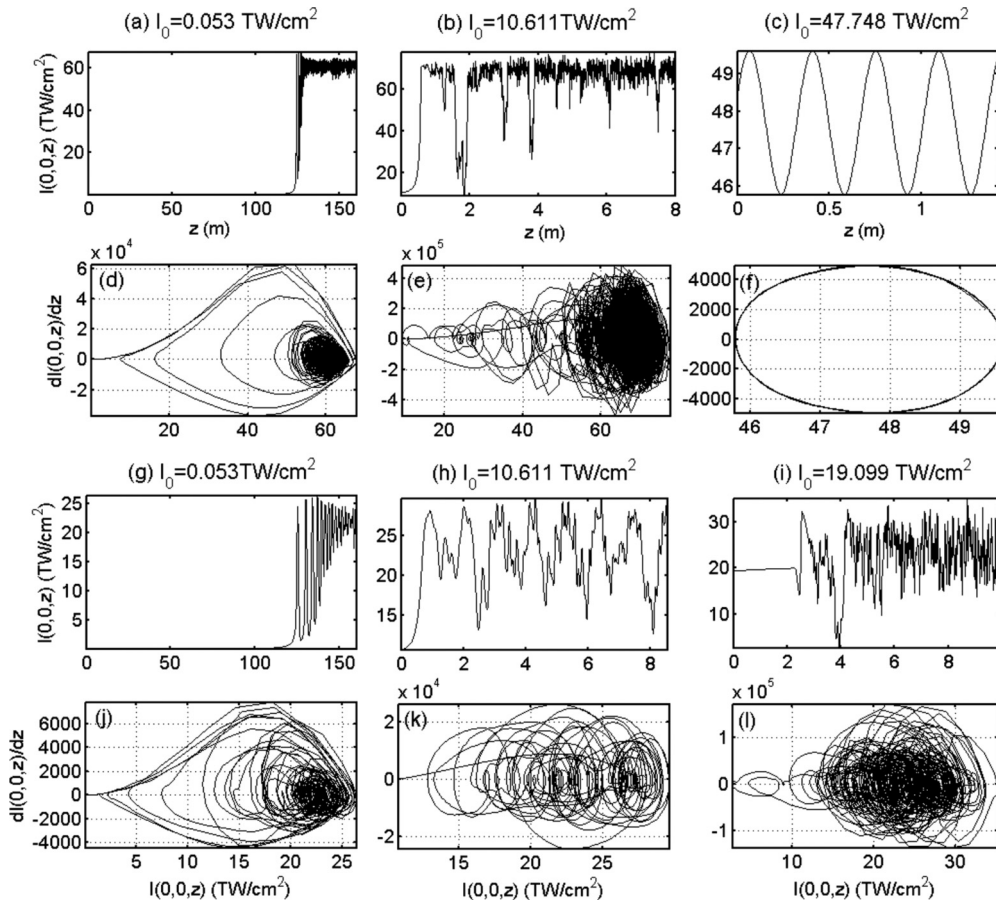

FIG. 7. Evolutions of laser fields at $(x,y) = 0$ [(a)–(c) and (g)–(i)] in two cases and corresponding phase space [(d)–(f) and (j)–(l)] with the same I_0 as given in Fig. 6. The upper two rows are for Case I and the bottom two rows are for Case II.
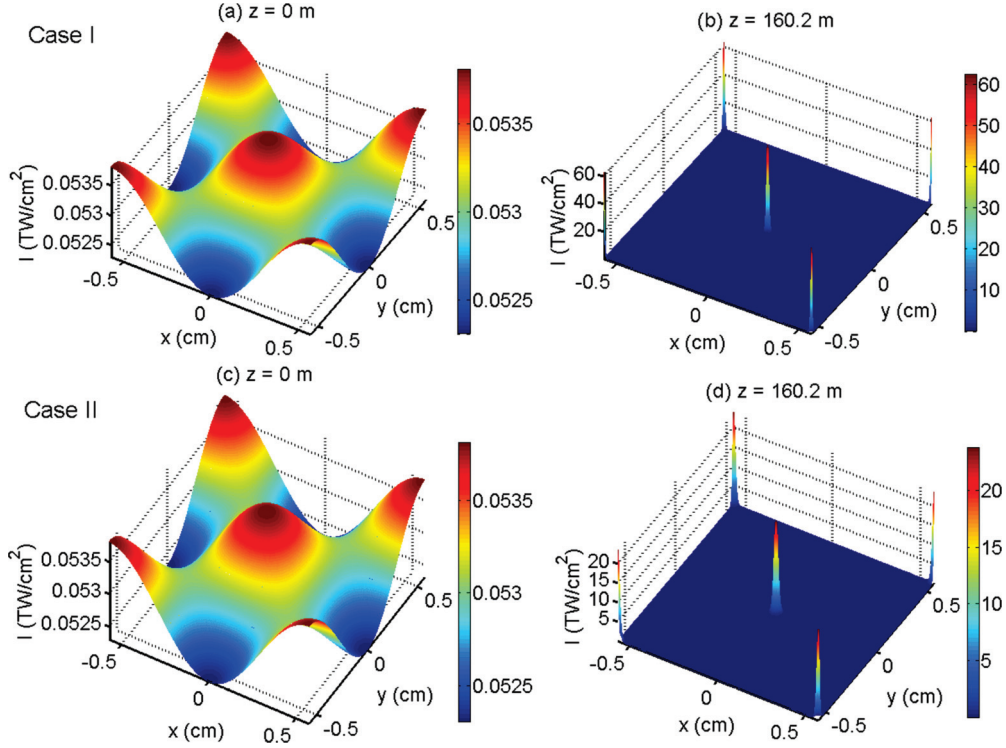
FIG. 8. (Color online) The transverse intensity patterns at different propagation distance in Case I [(a)–(b)] and Case II [(c)–(d)] with an initial laser intensity of $I_0 = 10I_{cr}$, which are corresponding to the points A and D shown in Fig. 6.

To have a clear comparison between the two different saturable effects, i.e, the plasma saturation effect and the higher-order Kerr nonlinear effects, in the following we consider two cases and refer to them as Case I and Case II. Case I corresponds to $\beta = 0$, and Case II corresponds to $\beta = -1$ in the nonlinear term $F(|E|^2)$ of Eq. (2). Thus, in Case I the Kerr terms are truncated to n_2 and the plasma saturation term is included; however, in Case II both the higher-order Kerr nonlinear effects and the plasma saturation effect are considered. Figure 6 shows the values of higher-order nonlinear terms relative to KF term and the most unstable growth rate of modulational instability Γ_{max} in Case I and Case II. It is shown that in the presence of HOKE for our parameter range, the high-order saturation term in Case II is much stronger than that in Case I for a wide range of intensities. In addition, Γ_{max} in Case I is about 4 times higher than that in Case II.

Figures 7–10 give the solutions of Eq. (2) in two different cases. At relatively low input intensity, say $10I_{cr}$ (see points A and D in Fig. 6), the high-order saturable effects are initially negligible. Equation (2) then reduces to the two-dimensional cubic NLSE that is not integrable. For the two-dimensional cubic NLSE, singular solutions would occur at the points of self-focusing, where the time of blowup is finite and the field intensities exhibit catastrophic processes [47,79–81]. As shown in Figs. 7(a) and 7(g), in both cases, the laser first experiences a focusing process and then energy in the laser fields would quickly converge into the filament structures shown in Figs. 8(b) and 8(d). However, the catastrophic process would be arrested by the defocusing effects arising from the plasma or higher-order Kerr nonlinearity with the increase of laser intensity. As a result, energy in the laser fields flows from

the filament regions to the peripheral regions, and, correspondingly, the peak laser intensity decreases. However, the laser power is still high and the focusing process occurs again. Such a process is the well-known multiple-refocusing phenomenon [50,84,85], which is clearly shown in Figs. 7(a) and 7(g). Their corresponding phase-space trajectories in Figs. 7(d) and 7(j) reveal an attractor-like structure. However, their irregular phase-space structures and the irregular distribution of energy in Fourier modes shown in Fig. 11(a) indicate a chaotic behavior. In addition, due to lower peak intensity in Case II, the filament size shown in Fig. 8(d) is larger than that in Case I, shown in Fig. 8(b).

When the initial laser intensity increases to $2000I_{cr}$ (see points B and E in Fig. 6), the high-order saturable effects cannot be neglected and the maximum growth rate of modulational instability quickly increases, as shown in Fig. 6. Figures 7(b) and 7(h) show that the laser field oscillates stochastically and the relevant phase-space trajectories also demonstrate stochastic behavior. On the other hand, we note from Fig. 9 that the characteristic scale length of the patterns in Case II is about 2 times larger than that in Case I. This can be understood from the relation $\lambda_{max} = 2\pi/\sqrt{\Gamma_{max}}$, where λ_{max} refers to the wavelength of the most unstable mode. In view of the curve for Γ_{max} in Fig. 6, one finds that the wavelength of modulational instability in Case II is approximately 2 times longer than that in Case I, leading to a large- or small-scale pattern structure in Cases II and I, respectively, as shown in Fig. 9.

With an increase of the initial laser intensity, in Case I a very interesting phenomenon is shown in Figs. 7(c) and 7(f). It is seen that when the laser intensity increases further
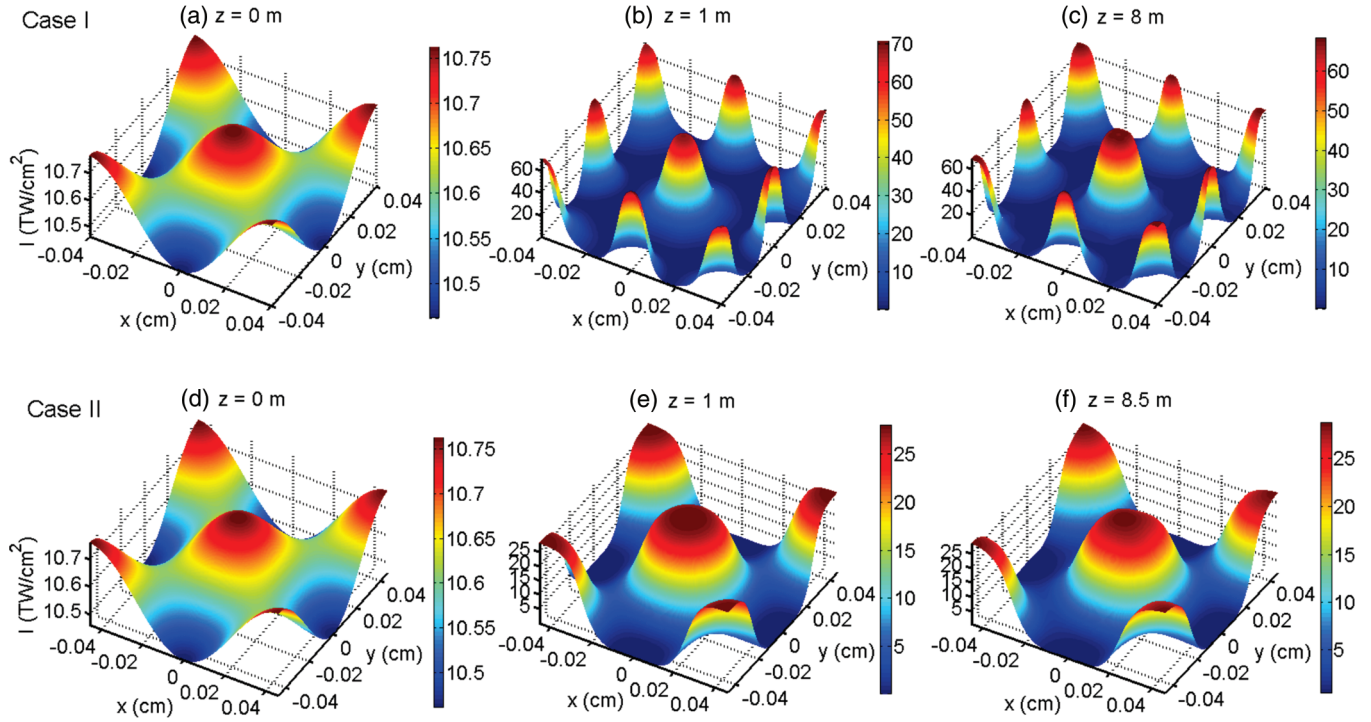
FIG. 9. (Color online) The transverse intensity patterns at different propagation distance in Case I [(a)–(c)] and Case II [(d)–(f)] with an initial laser intensity of $I_0 = 2000 I_{cr}$, which are corresponding to the points B and E shown in Fig. 6.

to $9000 I_{cr}$ (see point F in Fig. 6), pseudorecurrence [82] can appear. Actually, in this case nonlinear perturbation from the high-order saturation term becomes larger. However, the maximum growth rate of the modulational instability decreases sharply to zero in this region (see Fig. 6), which suggests that the instability cannot develop, eventually leading to the pseudorecurrent solution. Physically, we can consider that in this region plasma defocusing is strong enough to prevent the Kerr focusing singularity. In earlier works [47,82], pseudorecurrence was also observed when the saturation effect
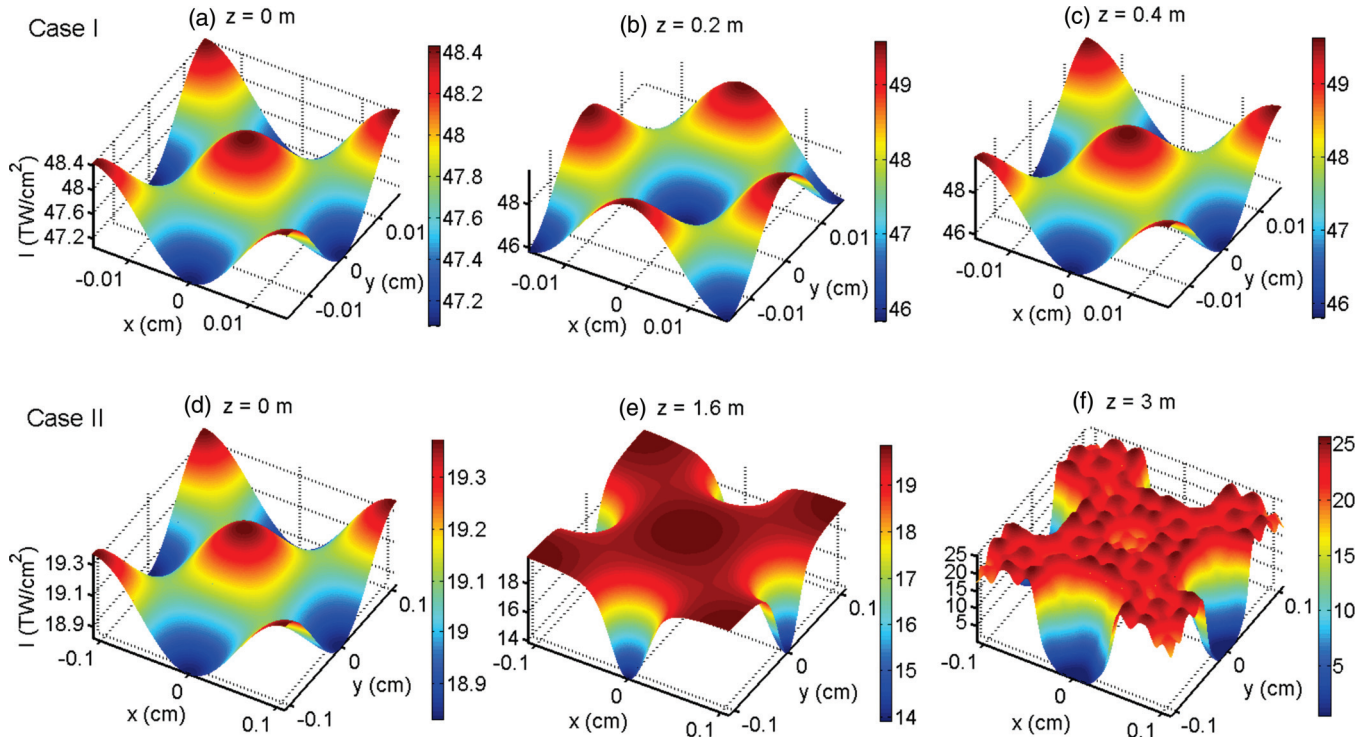

FIG. 10. (Color online) The transverse intensity patterns at different propagation distance in Case I [(a)–(c)] and Case II [(d)–(f)] with an initial laser intensity of $I_0 = 9000 I_{cr}$ and $I_0 = 3600 I_{cr}$, respectively, which correspond to the points C and F shown in Fig. 6.
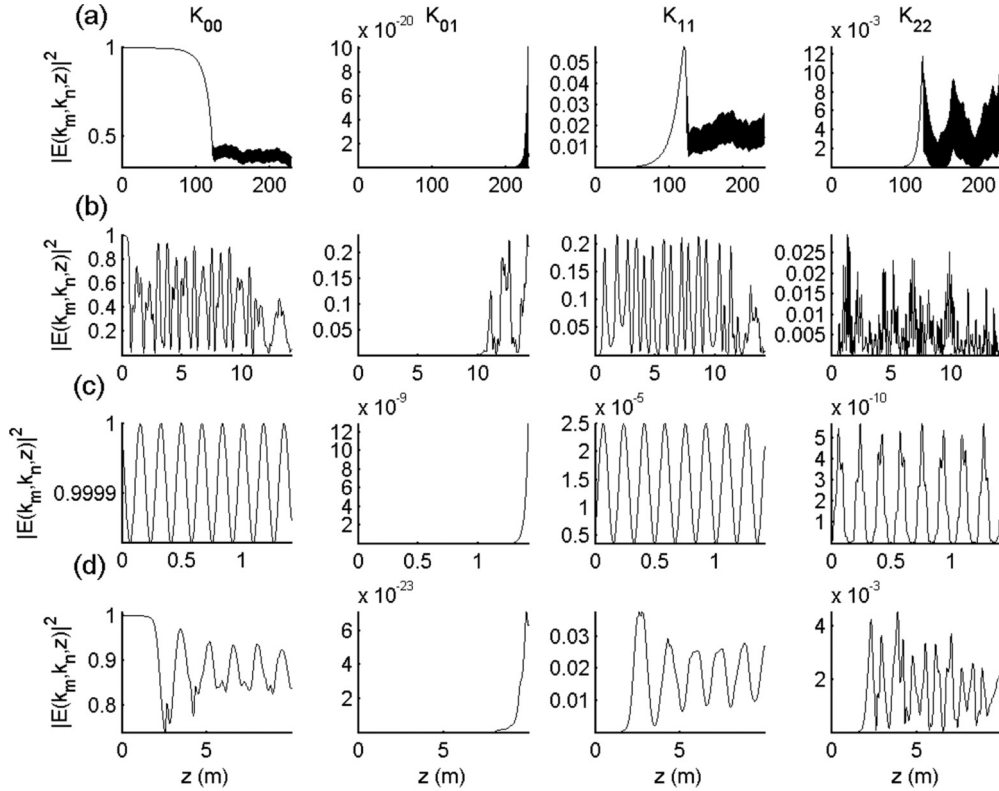
FIG. 11. The energy evolution in the Fourier modes with I_0, respectively, of $10I_{cr}$ (a), $2000I_{cr}$ (b), $9000I_{cr}$ (c) in Case I and $3600I_{cr}$ (d) in Case II.

was very strong and the modulational instability was weak. In contrast, for Case II, the strong HOKEs would induce a quite different behavior on the pattern dynamics, as shown in Figs. 7(i) and 7(l). Figure 10 shows the transverse intensity patterns at three appropriate propagation distances. We can see that in Case II, the laser fields first develop into a uniform X-type structure due to the modulational instability. Nevertheless, such uniform structures are quite unstable and small-scale turbulent structures quickly appear on this X-type pattern [86] as the laser propagates, which is in good agreement with the solution in the one-dimensional case, shown in Fig. 4(h). In addition, the complex interactions of these small-scale structures lead to the stochastic behavior of the laser evolution and phase-space trajectory shown in Figs. 7(i) and 7(l).

To clearly illustrate the mechanism that leads to the formation of these complicated patterns, we again investigate the evolution of energy contained in Fourier modes. In Fourier space, we can define the energy of system (2) as [70]

$$H = \sum_{K_{n,m}} H_{K_n, K_m} = \sum_{K_{n,m}} |E(K_n, K_m, z)|^2, \quad (10)$$

where $K_{n,m} = (K_n, K_m)$ represents the n-th Fourier mode in x space and the m-th mode in y space. The evolution of energy in the Fourier modes is shown in Fig. 11. Figure 11(a) corresponds to the condition of point D in Fig. 6 in Case I. It can be seen that as the laser propagates, the energy in the initial mode would slowly spread to higher diagonal modes at first, say K_{11} and K_{22}, and, correspondingly, the energy in the K_{11} and K_{22} modes increases. However, at the distance

$(z \approx 120$ m) where the peak laser intensity experiences a sharp increase [see Fig. 7(a)], the energy in the first three diagonal modes all decreases in a short propagation distance [see Fig. 11(a)], which implies that the energy in the system transfers from the high-order diagonal modes (K_{11} and K_{22}) to much higher-order diagonal modes. Physically, the energy in the laser fields would be concentrated on the higher-order or shorter-wavelength Fourier modes during the focusing process. Such process may be the intrinsic scheme of the formation of laser filament in air.

Figure 11(b) shows the case of point E in Fig. 6 in Case I. The stochastic evolution of energy in the high-order diagonal modes leads to the chaotic behavior of laser fields shown in Fig. 7(b). In particular, it is noted that for $z > 10$ m the energy in the diagonal modes decreases but in the nondiagonal modes increases. As a result, a considerable part of the energy lies in the nondiagonal Fourier modes. The abnormal partition of energy in Fourier modes would result in the formation of off-axis patterns [47]. Here, we do not show the off-axis patterns. It seems that such off-axis patterns are quite sensitive to the maximum growth rate of modulational instability. When the modulational instability is strong enough (a large Γ_{max}), the laser field would easily develop into these complicated patterns. The results in the one-dimensional case also verify this point.

We now discuss the pseudorecurrent case shown in Fig. 7(c). We see from Fig. 11(c) that the energy in the first two diagonal modes exhibits periodic motion but in high-order mode K_{22} is not exactly periodic, which indicates that the solution is pseudorecurrent rather than exactly recurrent as shown in Fig. 2(a) for the one-dimensional case. Figure 11(d)
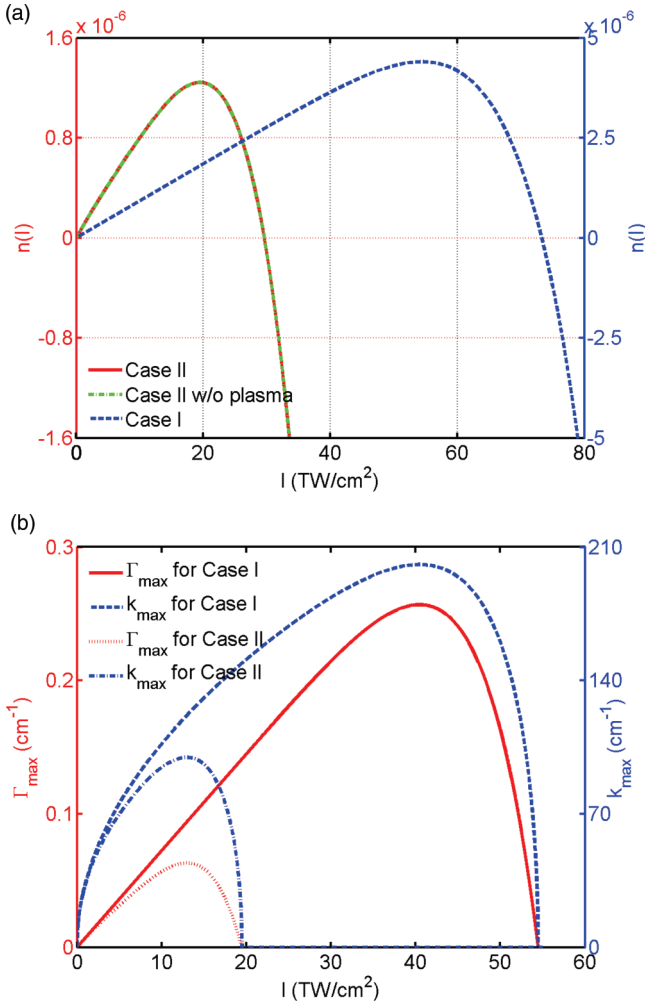
FIG. 12. (Color online) (a) Comparison of the nonlinear refractive index $n(I)$, where $n(I) = \frac{n_2}{\sqrt{3}}I - \frac{\gamma}{k_0}I^K$ in Case I and $n(I) = \Delta n - \frac{\gamma}{k_0}I^K$ in Case II. Here $\Delta n = \frac{n_2}{\sqrt{3}}I + \frac{n_4}{\sqrt{5}}I^2 + \frac{n_6}{\sqrt{7}}I^3 + \frac{n_8}{3}I^4$ is the nonlinear refractive index in Case II without the plasma. (b) Comparison of the most unstable growth rate of modulational instability Γ_{max} and the wave number of the most unstable modes in two cases, where $\Gamma_{max} = k_0 \frac{n_2}{\sqrt{3}}I - \gamma K I^K$ in Case I and $\Gamma_{max} = k_0(\frac{n_2}{\sqrt{3}}I + \frac{2n_4}{\sqrt{5}}I^2 + \frac{3n_6}{\sqrt{7}}I^3 + \frac{4n_8}{3}I^4) - \gamma K I^K$ in Case II, and the corresponding wave number of the most unstable modes satisfy the relation $k_{max} = \sqrt{2k_0\Gamma_{max}}$.

also shows the case of point C in Fig. 6 in Case II. It is found that the regular partition of energy in the first two diagonal modes dominates the main X-type structure shown in Fig. 10(e). However, the irregular behavior of energy in the high-order mode (K_{22}) leads to the appearance of the small-scale turbulent structures, as shown in Fig. 10(f). In addition, it can be seen from Figs. 11(c) and 11(d) that a small part of the energy is distributed in the nondiagonal mode (K_{01}); however, the ratio is still negligible compared with that in Fig. 11(b), which does not severely affect the symmetry of the intensity patterns, as seen in Fig. 10.

V. MULTIPLE FILAMENTATION SIMULATIONS

In the above sections, we have given a detailed comparison of nonlinear pattern dynamics in two different cases. Now we
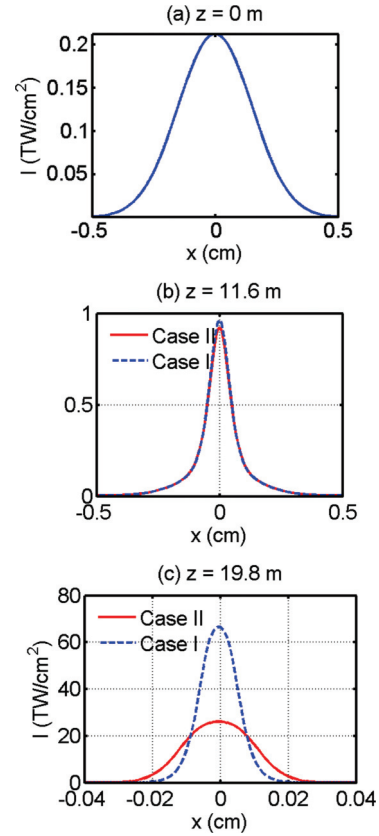

FIG. 13. (Color online) The intensity profile $I(x,0)$ at different propagation distances in two cases with an initial laser power of $P_{in} = 5P_{cr}$.

turn to the simulation of multiple filamentation of ultrashort laser. Filamentation has extensively been found in laser or particle beam propagations in air or plasmas [1–62,87]. As far as multiple filamentation of laser beams propagating in air is concerned, most of the numerical simulations are based on the so-called classical model where the plasma defocusing is considered as the saturating nonlinearity [48,54–58]. Here we analyze multiple filamentation of ultrashort laser pulses in air by comparing both plasma saturation effect and higher-order Kerr nonlinearities. Equation (1) in two-dimensional spaces is also solved using the standard spectral split-step scheme [47,70]. In the transverse directions, a fixed grid of high resolution ($\Delta x = \Delta y \leqslant 20\,\mu m$) is taken. A sufficiently large simulation box [($L_x, L_y) \geqslant 6w_0$] guarantees free propagation of the laser pulse [48]. The input laser beam is modeled by a super-Gaussian profile

$$E(x,y,z=0) = \sqrt{\frac{2P_{in}}{\pi w_0^2}}\exp\left[-\frac{x^2+y^2}{w_0^2}\right]^m, \quad (11)$$

where P_{in} is the input laser power, w_0 is the initial beam waist, and m is the index to define the super-Gaussian beam with $m = 1$ corresponding to a Gaussian beam. In our simulations, we consider the initial beam waist as 0.3 cm and the input laser power on a level of low ($P_{in} = 5P_{cr}$), moderate ($P_{in} = 80P_{cr}$), and high ($P_{in} = 1000P_{cr}$) powers, respectively, and $m = 1$ is assumed in the simulations. In addition, the propagation medium is assumed to be O_2.
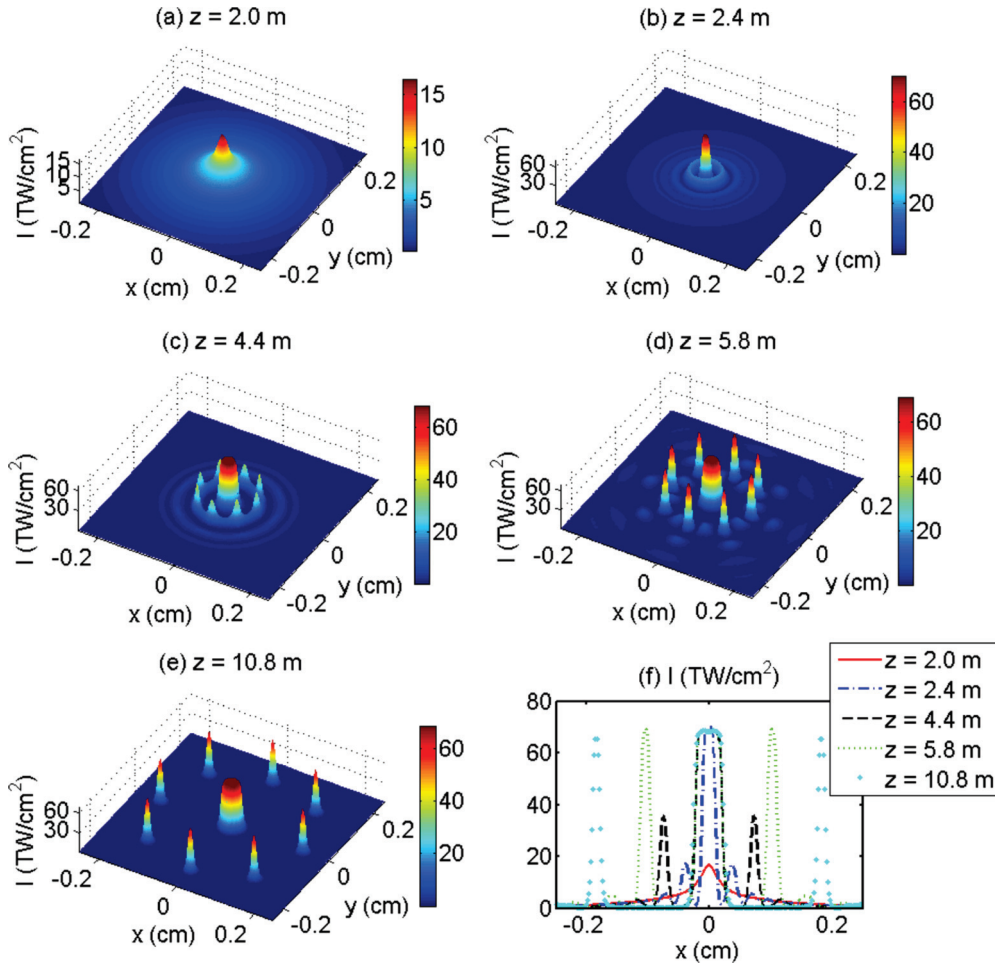
FIG. 14. (Color online) The transverse intensity patterns at different propagation distance in Case I [(a)–(e)] with a laser power of $P_{in} = 80P_{cr}$ and the corresponding intensity profiles (f) at $y = 0$, where the displayed space scale is 0.5×0.5 cm (scale of the simulation box is 2×2 cm).

Figure 12 shows the nonlinear refractive index $n(I)$ and the most unstable growth rate Γ_{max} of the modulational instability of a plane wave [51,85,88] in Case I and Case II as defined in Sec. IV. With the increase of laser intensity, it can be seen that the total nonlinear refractive index decreases from positive to negative values. Particularly, intensity clamping occurs when the total nonlinear refractive index equals zero [89–91]. However, it is necessary to mention that intensity clamping depends much on the focusing condition of the laser beam, which may result in a champing intensity that does not correspond to the zero value of the total nonlinear refractive index [92–95]. It can be seen from Fig. 12 that Case II yields a lower intensity for $n(I) = 0$, which directly determines a lower peak intensity in laser filaments in Case II and is in excellent agreement with the simulation results (28.6 TW/cm^2 vs 72.9 TW/cm^2) shown in Figs. 14 and 15. In addition, Γ_{max} in Case I is about 4 times higher than that in Case II, leading to faster formation of filaments in Case I (see Figs. 14 and 15). Figure 12(b) also shows that the wave number of the most unstable modes in Case I is much larger than that in Case II, demonstrating that the propagation of ultrashort laser in air in Cases I and II is dominated by a short- and long-wavelength modulation, respectively.

Figure 13 shows the process of single filament formation in the two cases for a low laser power of $5P_{cr}$. In both cases, the laser profiles collapse towards a well-known "Towns profile" [see Fig. 13(b)] during the first self-focusing stage [96,97]. At this time, the saturable defocusing effects do not take effect yet. Therefore, "Towns Profiles" in the two cases are almost the same, as shown in Fig. 13(b). With the increase of laser intensity, the plasmas are generated or HOKEs come into play. Then the triggered defocusing effects will counteract the focusing effect and arrest the spatial collapse of the laser beam. Finally, the balance between the focusing effects and defocusing effects sets a limit of the minimum beam diameter and the highest intensity. The final equilibrium state of the laser beam corresponds to the formation of single laser filament. Figure 13(c) shows the intensity profile of the laser filament in the two cases. It can be seen that the filament in Case II has a wider diameter (254 μm vs 138 μm) but a lower peak intensity (26.07 TW/cm^2 vs 66.47 TW/cm^2) than that in Case I, which is basically consistent with the points of $n(I) = 0$.

We now consider the case of multiple filament formation with the initial laser power of $80P_{cr}$. Figures 14 and 15 show the phase of multiple filament formation and propagation in the two cases. As illustrated above, the laser would first evolve
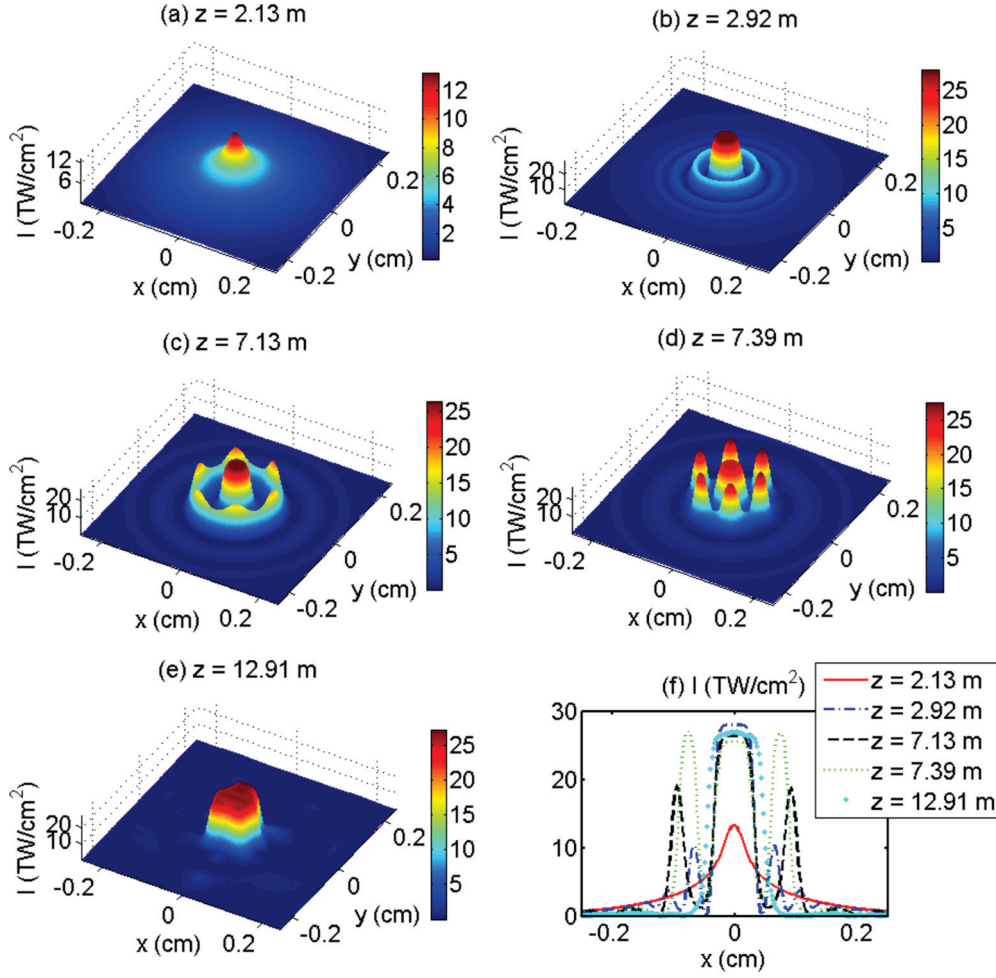
FIG. 15. (Color online) The transverse intensity patterns at different propagation distance in Case II [(a)–(e)] with a laser power of $P_{in} = 80 P_{cr}$ and the corresponding intensity profiles (f) at $y = 0$, where the displayed space scale is 0.5×0.5 cm (scale of the simulation box is 2×2 cm).

to the "Towns profile" [see Figs. 14(a) and 15(a)], which is the typical characteristic for a Gaussian beam [96,97]. Then the defocusing effects arising from the plasma or higher-order Kerr nonlinear effects counteract the optical self-focusing by diverging into a series of concentric ring structures [see Figs. 14(b) and 15(b)], as have been observed in existing experiments and numerical simulations [98–102]. The ring structures may result from the interference of the convergent background field and the divergent field due to the reflection of the front part of the pulse from the surface [98,99]. One the other hand, we note from Fig. 18 that before the occurrence of filaments, there exists an oscillation between the central focal spot and the ring structures. Such an interesting phenomenon has also been observed in previous work [100], which could be due to the competition between the convergent field and divergent field. Finally, only the interior ring with higher refractive index can quickly break up into narrow filaments by the modulational instability [see Figs. 14(c) and 15(c)]. The formation and breakup of the ring structures have also been observed for intense lasers in near-critical plasmas by use of three-dimensional particle-in-cell simulations [103]. Thus, the appearance and breakup of the ring structures should

be a typical characteristic to multiple filamentation of lasers propagating in the medium. Furthermore, Figs. 14(d) and 15(d) show that the interactions among the filaments differ markedly in the two cases. In Case I, propagation of the external filaments exhibits transverse deflection [see Figs. 14(e) and 18(a)], as observed in some previous experiments [48]. On the contrary, in Case II, the filaments rapidly coalesce to a central core, resulting in a thick light bullet [see Figs. 15(e) and 18(b)]. The mechanism of the two different propagation modes can be understood in terms of the evolution of the overall mean-square radius $\langle r_\perp^2 \rangle$ of the beam. For our conservative system (1), we can rewrite the evolution equation for $\langle r_\perp^2 \rangle$ as [85]

$$P d_z^2 \langle r_\perp^2 \rangle = 8 \left\{ H + \int [2F(|E|^2) - f(|E|^2)|E|^2] d\vec{r} \right\}, \quad (12)$$

where $P = \int |E|^2 d\vec{r}$ is the laser power, $\langle r_\perp^2 \rangle$ is defined as $\int r_\perp^2 |E|^2 d\vec{r} / P$, $H = \int [\frac{1}{2k_0 n_0}(|\partial_x E|^2 + |\partial_y E|^2) - F(|E|^2)] d\vec{r}$ is the Hamiltonian of the system (1), $F(|E|^2) \equiv \int_0^{|E|^2} f(s) ds$, $f(s) = k_0 \Delta n(s) - \gamma s^K$, and $s = |E|^2$. For two or more in-phase filaments with a mean separation distance δ, the Hamiltonian H can be expanded as $H = H_{free} + H_{int}(\delta)$, where

H_{free} refers to the contribution of each individual filament and $H_{\text{int}}(\delta)$, which decreases exponentially with δ^2 (see Ref. [85] for more details), describes the interaction between the filaments. In addition, the critical separation distance δ_c, below which the filaments can coalesce, is given by the zeros of the right-hand side of Eq. (12). When the separation distance is above δ_c, no mutual attraction between the filaments is possible and the filamentation would develop independently [85,104]. In the two cases, it is found that in Case II δ_c is larger than that in Case I. Moreover, due to a larger waist (ρ) of filaments in Case II, the relative separation distance (δ/ρ) of the filaments in Case II is smaller than that in Case I, which suggests that the filaments in Case II are easier to attract each other. Accordingly, in Case I no mutual attraction is observed for filaments at wider separation distances. Instead, the filaments diverge along the divergent tide from the reflection part of the pulse. However, in Case II, filaments with small ($\delta < \delta_c$) separation distances can provide strong attraction force to seize the divergent tide and turn to a fusion process, which enhances the channel stability and leads to prolongation of the propagating distance [24,48]. In order to illustrate the robustness of the two different propagation modes, we further do the simulation by choosing some neighboring parameters. It is found that for $90P_{\text{cr}}$ and $100P_{\text{cr}}$, the similar characteristics analyzed above can also occur. In addition, it is interesting to note that the propagation dynamics of laser beams shown in Figs. 14 and 15 are very similar to the behavior of spatial solitons, including the breakup of high-order solitons and the interaction dynamics of different solitons [105]. In fact, such solitonlike dynamics are the typical characteristics of our reduced model [48], especially for the conservative case.

Figure 17, which is for a much higher laser power, namely $P_{\text{in}} = 1000P_{\text{cr}}$, shows the intensity patterns for the two cases at appropriate propagation distances. From Fig. 16(a) we see that the initial refractive index in the central region satisfies $n(I) > 0$ in Case I but $n(I) < 0$ in Case II. Accordingly, in Case II the laser first experiences defocusing, especially when $n(I)$ is near the minimum, and energy of the laser fields would flow into the region with maximum refractive index that corresponds to $dn/dr = 0$ [see Fig. 17(e)]. As a result, higher-order Kerr nonlinear effects produce a deep hole in the transverse intensity distribution and most of the light energy is accumulated in a cylindrical optical channel, shown as the thick (red) ring in Fig. 17(f). Differing from the unstable rings shown in Figs. 14 and 15, such a channel, which can trap the intense laser light for several meters, as can be seen in Fig. 18(d), corresponds to $n(I) \approx 0$ and can make the system become more compact. From Fig. 17(f) we can also see that rings are formed outside as well as inside the channel due to the defocusing effects acting on this channel. Figures 17(g) and 17(h) show that only the inside rings would break up into filaments and then merge with the optical channel. It can also be seen that small-scale turbulent structures appear in the optical channel [see Figs. 17(g) and 17(h)], but they do not affect the robustness of the channel. Such local complex structures may be characteristic of Case II, also discussed in Secs. III and IV, and can be attributed to energy distribution among the small-scale Fourier modes typical for localized turbulence and chaos [66,70,106]. On the other hand, in Case I filaments emerge from the rings outside
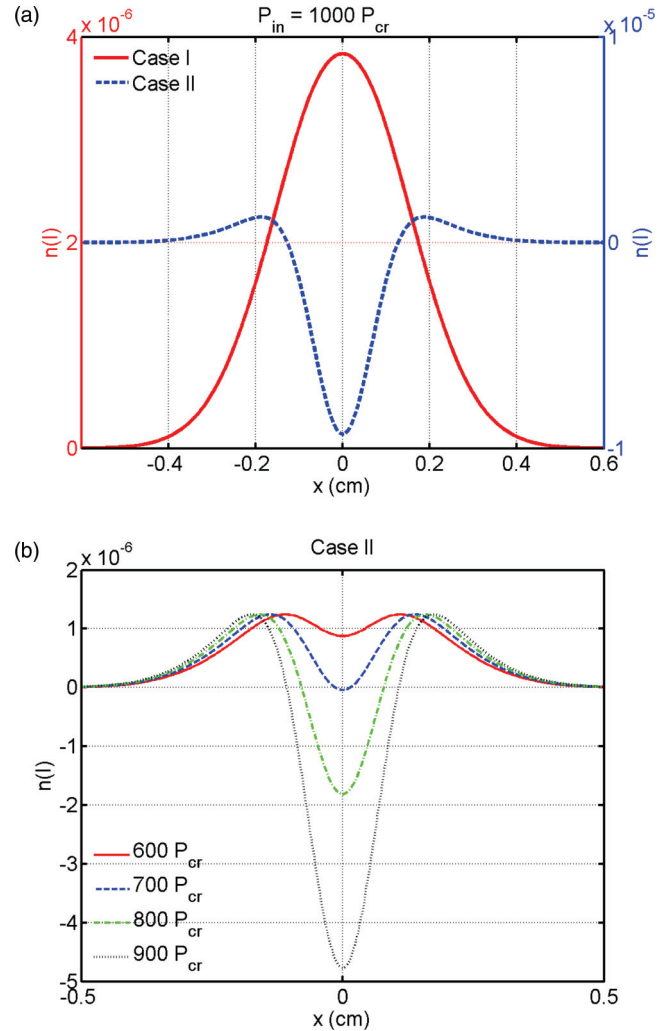

FIG. 16. (Color online) The initial refractive index distribution along the axis of $y = 0$ for the two cases with a laser power of $P_{\text{in}} = 1000P_{\text{cr}}$ (a) and the initial refractive index distribution in Case II at different input powers (b).

a central optical pillar [see Figs. 17(a) and 17(b)]. As the laser propagates, the interior filaments would redistribute due to mutual attraction. However, the exterior filaments would move outwards along with the divergent tide, as shown in Figs. 17(c) and 17(d). Figure 16(b) shows the initial refractive index at different input powers in Case II. We can see that the location of maximum refractive index deviate from the central spot and the deviation increases with the the input power, which could result in the formation of optical channel with variable radius. Thus, in our parameter range the channel structure appears to be typical in Case II at very high input powers ($\geqslant 600P_{\text{cr}}$). Since the characteristic scale length of the system differs significantly when different mechanisms, such as the ones considered here for our parameter range, of filamentation are in operation, experimental records of the spatial filament patterns would possibly be a new basis for identifying the regime of filamentation in terawatt laser propagation in air. However, we should mention that our simulation results as given in Figs. 14–18 are mainly based on the measurement
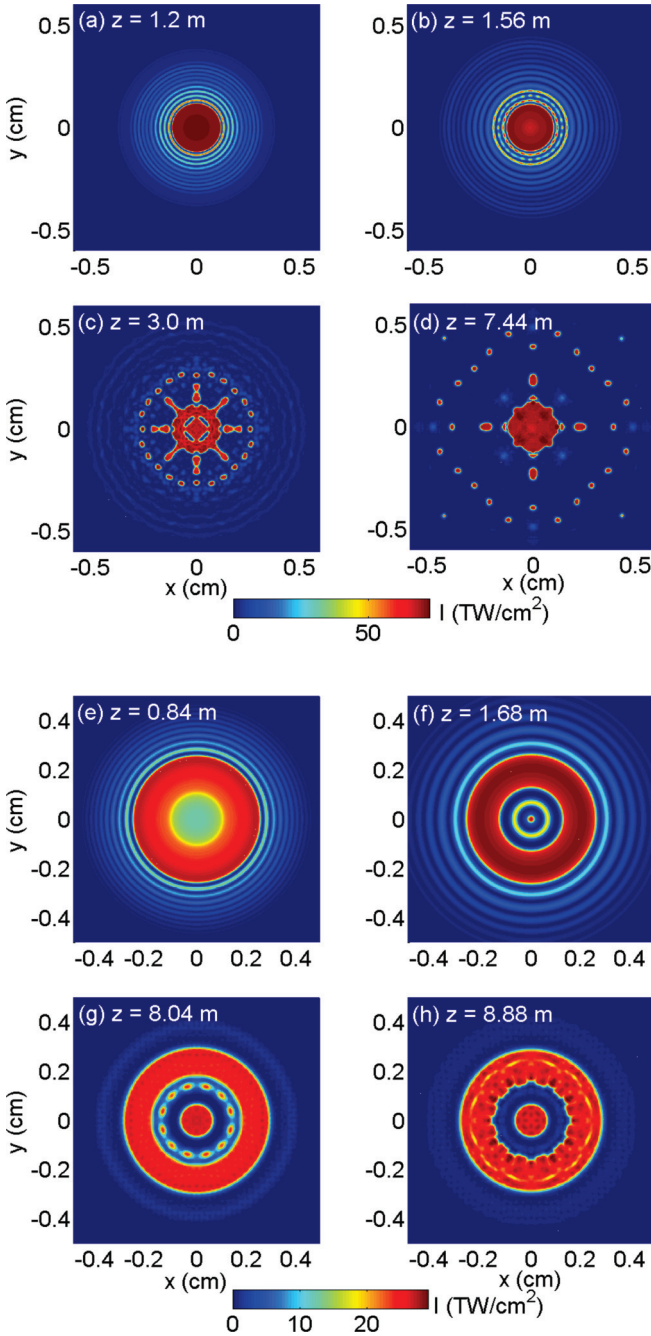
FIG. 17. (Color online) The transverse laser intensity patterns at different propagation distance in Case I [(a)–(d)] and Case II [(e)–(h)] with a laser power of $P_{\text{in}} = 1000P_{\text{cr}}$, where the displayed space scale is 1.2×1.2 cm in Case I and 1.0×1.0 cm in Case II (scale of the simulation box is 3×3 cm).

FIG. 18. (Color online) The laser intensity profile $I(x,0,z)$ along the propagation direction at two cases; the top row is for $P_{\text{in}} = 80P_{\text{cr}}$ and the bottom row is for $P_{\text{in}} = 1000P_{\text{cr}}$.

data (as shown in Tables I and II). To observe these different filamentation patterns experimentally, they possibly have to follow the specific values of parameters and experimental conditions as discussed in Ref. [25].

The difference in the results for the two cases considered here originates from the characteristics of the modulational instability. The modulational instability growth rate of a plane wave given by Eq. (1) can be expressed as $\Gamma = k\sqrt{f'(I_0)I_0 - k^2/(4k_0^2)}$, where $f(I_0) = k_0 \Delta n(I_0) - \gamma I_0^K$ and
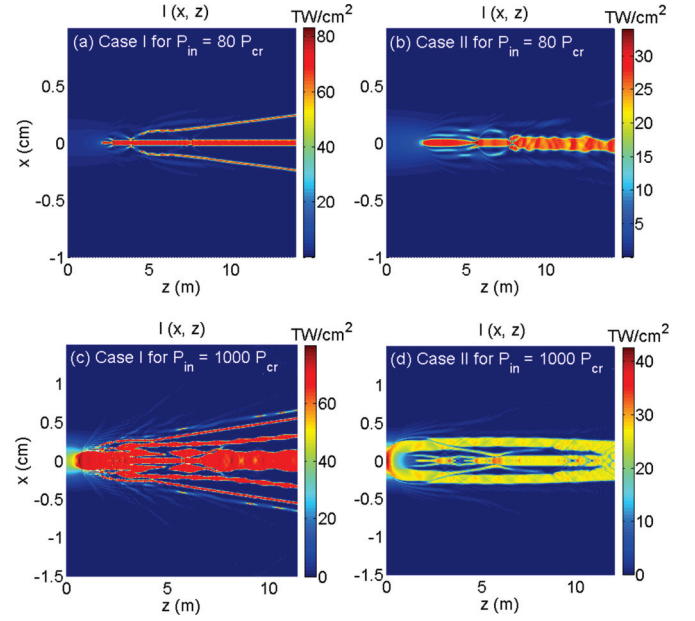
I_0 is the incident laser intensity. The corresponding wave number of the most unstable mode is $k_{\max} = k_0\sqrt{2f'(I_0)I_0}$, and it satisfies the relation $k_{\max} = \sqrt{2k_0\Gamma_{\max}}$. In view of the curve for $k_{\max}$ in Fig. 12(b), it can be seen that the wave number of modulational instability in Case I is much larger than that in Case II. That is, in Cases I and II the laser propagation suffers mainly from short- and long-wavelength modulation, which leads to a smaller and larger filament size, respectively, as shown in Figs. 14 and 15. As a result, the short-wavelength modulation in Case I leads to formation of small-scale filaments, and the long-wavelength modulation in Case II leads to a thick optical bullet. Figure 12(a) also shows that neglect of the high-order plasma saturation term in Case II does not significantly affect the beam dynamics, demonstrating that the higher-order Kerr nonlinear effect would become important in the context of our specific parameters. This is expected, since in our parameter range the peak laser intensity always remains below 4×10^{13} W/cm^2 in Case II, but in Case I plasma defocusing can counteract Kerr focusing [101] for $I \geqslant (\frac{n_2k_0}{\sqrt{3}K\gamma})^{1/(K-1)} \approx 5.4 \times 10^{13}$ W/cm^2. In addition, our estimations here is qualitatively consistent with the parameter range demonstrated in Refs. [40,41,45,46], where it was concluded that the filamentation process is dominated by plasma for long pulses at short wavelengths and by HOKEs for short pulses at long wavelengths. Finally, we should give a brief discussion on the effect of noise. In our further simulations, we have added a small noise level in Eq. (11). It is found that the filament patterns, as shown in Figs. (14), (15), and 17, can be kept when the noise level is very small. In particular, for very high powers ($\geqslant 600P_{\text{cr}}$), the filament patterns shown in Fig. 17 are quite robust, even when subjected to a high noise level.

VI. SUMMARY AND DISCUSSION

In summary, we have systematically investigated the non-linear pattern dynamics and multiple filamentation of terawatt laser pulses in air by using a generalized saturable nonlinear Schrödinger equation including a high-order plasma saturation term without and with HOKEs. In the one-dimensional case, the latter is investigated in detail for O_2 and N_2. Our theoretical and numerical results show that the Hamiltonian perturbation induced by the plasma and/or higher-order Kerr nonlinearity can destroy the coherent propagation of the laser and result in spatially complex incoherent structures. In the context of the specific parameters used here, it is found that higher-order Kerr nonlinearity can lead to quite different behaviors of the pattern dynamics in both one- and two-dimensional spaces, where turbulent small-scale spatial structures rapidly appear as the laser propagates in air. In particular, in the one-dimensional case, for N_2 with our parameter choice, the higher-order Kerr nonlinearity cannot always provide the negative contribution to the refractive index in the regime $4.49 \times 10^{12} < I_0 (\text{W/cm}^2) < 2.74 \times 10^{13}$ that is needed to balance the KF. As a result, in the regime $4.49 \times 10^{12} < I_0 (\text{W/cm}^2) < 1.91 \times 10^{13}$, where the focusing term $\beta_6 |E|^6$ in HOKE gives a large perturbation term and the system becomes rather unstable (a large $\Gamma_{\max}$), a typical chaotic behavior that is associated with a continuous phase shift and complicated spatial structures is shown and its phase-space trajectory corresponds to the formation of irregular HMO crossings. Our Fourier mode analyses further confirm that the spatially complicated structures are associated with the stochastic evolution of energy in higher-order, or shorter-wavelength, modes. For the two-dimensional case, our numerical results demonstrate that the oscillation filamentation, chaotic evolution, spatial complicated patterns, and pseudorecurrence can appear with increase of the saturable nonlinear effects in Case I where the Kerr terms are truncated to n_2. We find that the filamentation corresponds to concentrations of energy in shorter-wavelength diagonal modes, and the pseudorecurrence phenomenon occurs only when the saturation effects are strong enough.

Furthermore, our results on the multiple filamentation shows that in our parameter range for laser pulses at moderate power levels, plasma saturation effects can lead to production of more small-scale filament structures, but higher-order Kerr nonlinearity can lead to different filamentation patterns and produce a thick optical bullet. At much higher powers, a typical optical channel, capable of conveying a high-power laser for a long distance, can be generated if the higher-order Kerr nonlinearity is included. Such a different behavior induced by the latter can enhance the long-distance propagation of the laser. Because a wave beam with a small perturbation can be developed into very rich localized pattern structures by the modulational instability, such local structures may be the early form of filament formation. The formation of different nonlinear structures of laser fields propagating in air would eventually evolve into complex filamentation patterns, as shown in our results. Their corresponding nonuniformities in the beam profile can be attributed to the stochastic evolution of the shorter-wavelength modes (or higher-order Fourier modes), where strong mode-mode interactions triggered by the nonlinear saturable effects may enlarge the local inhomo-geneities on the beam profile and modulational instability can broaden the frequency spectrum of the incident laser. In particular, for self-focusing, the energy spectrum of the laser should experience a transition from the long-wavelength modes to the shorter-wavelength ones. For different nonlinear effects, different pattern structures and filamentation phenomena of femtosecond terawatt laser pulses in air therefore can appear due to the nonlinear evolution of these localized structures by the modulational instability.

[1] B. L. Fontaine, F. Vidal, Z. Jiang, C. Y. Chien, D. Comtois, A. Desparois, T. W. Johnston, J. C. Kieffer, H. Pépin, and H. P. Mercure, Phys. Plasmas **6**, 1615 (1999).

[2] P. Rairoux, H. Schillinger, S. Niedermeier, M. Rodriguez, F. Ronneberger, R. Sauerbrey, B. Stein, D. Waite, C. Wedekind, H. Wille, L. Wöste, and C. Ziener, Appl. Phys. B **71**, 573 (2000).

[3] A. Biswas, Appl. Maths. Comput. **153**, 369 (2004); Chaos Solitons Fractals **14**, 673 (2002).

[4] L. Bergé and S. Skupin, Phys. Rev. Lett. **100**, 113902 (2008).

[5] X. M. Zhao, J.-C. Diels, C. Y. Wang, and J. M. Elizondo, IEEE J. Quantum Electron. **31**, 599 (1995).

[6] L. Wöste, C. Wedekind, H. Wille, P. Rairoux, B. Stein, S. Nikolov, C. Werner, S. Niedermeier, F. Ronneberger, H. Schillinger, and R. Sauerbrey, Laser Optoelektron. **29**, 51 (1997).

[7] A. Couairon, Eur. Phys. J. D **27**, 159 (2003).

[8] A. Couairon, J. Biegert, C. P. Haurt, W. Kornells, F. W. Helbing, U. Keller, and A. Mysyrowicz, J. Mod. Opt. **53**, 75 (2006).

[9] C. P. Hauri, W. Kornelis, F. W. Helbing, A. Heinrich, A. Couairon, A. Mysyrowicz, J. Biegert, and U. Keller, Appl. Phys. B **79**, 673 (2004).

[10] J. R. Peñano, P. Sprangle, B. Hafizi, A. Ting, D. F. Gordon, and C. A. Kapetanakos, Phys. Plasmas **11**, 2865 (2004).

[11] I. Alexeev, A. Ting, D. F. Gordon, E. Briscoe, J. R. Penano, R. F. Hubbard, and P. Sprangle Appl. Phys. Lett. **84**, 4080 (2004).

[12] A. Braun, G. Korn, X. Liu, D. Du, J. Squier, and G. Mourou, Opt. Lett. **20**, 73 (1995).

[13] J. Kasparian, J. Wolf, Y. B. André, G. Méchain, G. Méjean, B. Prade, P. Rohwetter, E. Salmon, K. Stelmaszczyk, J. Yu, A. Mysyrowicz, R. Sauerbrey, L. Woeste, and J. P. Wolf, Opt. Express **16**, 466 (2008).

[14] J. Kasparian, M. Rodriguez, G. Mejean, J. Yu, E. Salmon, H. Wille, R. Bourayou, S. Frey, Y.-B. André, A. Mysyrowicz,

R. Sauerbrey, J. P. Wolf, and L. Wöste, Science **301**, 61 (2003).

[15] E. T. J. Nibbering, P. F. Curley, G. Grillon, B. S. Prade, M. A. Franco, F. Salin, and A. Mysyrowicz, Opt. Lett. **21**, 62 (1996).

[16] H. Yang, J. Zhang, J. Zhang, L. Z. Zhao, Y. J. Li, H. Teng, Y. T. Li, Z. H. Wang, Z. L. Chen, Z. Y. Wei, J. X. Ma, W. Yu, and Z. M. Sheng, Phys. Rev. E **67**, 015401 (2003).

[17] J. M. Dai, X. Xie, and X. C. Zhang, Phys. Rev. Lett. **97**, 103903 (2006).

[18] H. Zhong, N. Karpowicz, and X. C. Zhang, Appl. Phys. Lett. **88**, 261103 (2006).

[19] C. D'Amico, A. Houard, M. Franco, B. Prade, A. Mysyrowicz, A. Couairon, and V. T. Tikhonchuk, Phys. Rev. Lett. **98**, 235002 (2007).

[20] C. D'Amico, A. Houard, S. Akturk, Y. Liu, J. L. Bloas, M. Franco, B. Prade, A. Couairon, V. T. Tikhonchuk, and A. Mysyrowicz, New J. Phys. **10**, 013015 (2008).

[21] L. V. Keldysh, Zh. Eksp. Teor. Fiz. **47**, 1945 (1964) [Sov. Phys. JETP **20**, 1307 (1965)].

[22] V. I. Bespalov and V. I. Talanov, Zh. Eksp. Teor. Fiz. Pis'ma Red. **3**, 471 (1966) [JETP Lett. **3**, 307 (1966)].

[23] M. Mlejnek, M. Kolesik, J. V. Moloney, and E. M. Wright, Phys. Rev. Lett. **83**, 2938 (1999).

[24] T. T. Xi, X. Lu, and J. Zhang, Phys. Rev. Lett. **96**, 025003 (2006).

[25] V. Loriot, E. Hertz, O. Faucher, and B. Lavorel, Opt. Express **17**, 13429 (2009); **18**, 3011 (2010).

[26] A. Couairon, Phys. Rev. A **68**, 015801 (2003).

[27] N. Aközbek, C. M. Bowden, A. Talebpour, and S. L. Chin, Phys. Rev. E **61**, 4540 (2000).

[28] N. Aközbek, M. Scalora, C. M. Bowden, and S. L. Chin, Opt. Commun. **191**, 353 (2001).

[29] M. Kolesik, D. Mirell, J.-C. Diels, and J. V. Moloney, Opt. Lett. **36**, 3685 (2010).

[30] Y.-H. Chen, S. Varma, T. M. Antonsen, and H. M. Milchberg, Phys. Rev. Lett. **105**, 215005 (2010).

[31] J. K. Wahlstrand, Y.-H. Cheng, Y.-H. Chen, and H. M. Milchberg, Phys. Rev. Lett. **107**, 103901 (2011).

[32] P. Polynkin, M. Kolesik, E. M. Wright, and J. V. Moloney, Phys. Rev. Lett. **106**, 153902 (2011).

[33] J. M. Brown, E. M. Wright, J. V. Moloney, and M. Kolesik, Opt. Lett. **37**, 1604 (2012).

[34] P. Béjot, J. Kasparian, S. Henin, V. Loriot, T. Vieillard, E. Hertz, O. Faucher, B. Lavorel, and J. P. Wolf, Phys. Rev. Lett. **104**, 103903 (2010).

[35] M. Petrarca, Y. Petit, S. Henin, R. Delagrange, P. Béjot, and J. Kasparian, Opt. Lett. **37**, 4347 (2012).

[36] A. Couairon and A. Mysyrowicz, Phys. Rep. **441**, 47 (2007).

[37] S. L. Chin, S. A. Hosseini, W. Liu, Q. Luo, F. Théberge, N. Aközbek, A. Becker, V. P. Kandidov, O. G. Kosareva, and H. Schroeder, Can. J. Phys. **83**, 863 (2005).

[38] S. Tzortzakis, M. A. Franco, Y.-B. Andre, A. Chiron, B. Lamouroux, B. S. Prade, and A. Mysyrowicz, Phys. Rev. E **60**, 3505(R) (1999).

[39] O. Kosareva, J. Daigle, N. Panov, T. J. Wang, S. Hosseini, S. Yuan, G. Roy, V. Makarov, and S. L. Chin, Opt. Lett. **36**, 1035 (2011).

[40] V. Loriot, P. Béjot, W. Ettoumi, Y. Petit, J. Kasparian, S. Henin, E. Hertz, B. Lavorel, O. Faucher, and J. Wolf, Laser Phys. **21**, 1319 (2011).

[41] P. Béjot, E. Hertz, J. Kasparian, B. Lavorel, J. P. Wolf, and O. Faucher, Phys. Rev. Lett. **106**, 243902 (2011).

[42] H. T. Wang, C. Y. Fan, P. F. Zhang, C. H. Qiao, J. H. Zhang, and H. M. Ma, Opt. Express **18**, 24301 (2010).

[43] H. T. Wang, C. Y. Fan, P. F. Zhang, C. H. Qiao, J. H. Zhang, and H. M. Ma, J. Opt. Soc. Am. B **28**, 2081 (2011).

[44] W. Ettoumi, P. Béjot, Y. Petit, V. Loriot, E. Hertz, O. Faucher, B. Lavorel, J. Kasparian, and J. P. Wolf, Phys. Rev. A **82**, 033826 (2010).

[45] H. T. Wang, C. Y. Fan, H. Shen, P. F. Zhang, and C. H. Qiao, Opt. Commun. **293**, 113 (2012).

[46] C. Brée, A. Demircan, and G. Steinmeyer, Phys. Rev. A **85**, 033806 (2012).

[47] C. T. Zhou, X. T. He, and T. X. Cai, Phys. Rev. E **50**, 4136 (1994); C. T. Zhou and X. T. He, *ibid*. **49**, 4417 (1994); X. T. He and C. T. Zhou, J. Phys. A **26**, 4123 (1993).

[48] S. Skupin, L. Bergé, U. Peschel, F. Lederer, G. Méjean, J. Yu, J. Kasparian, E. Salmon, J. P. Wolf, M. Rodriguez, L. Wöste, R. Bourayou, and R. Sauerbrey, Phys. Rev. E **70**, 046602 (2004).

[49] B. Qiao, C. T. Zhou, and C. H. Lai, Appl. Phys. Lett. **91**, 221114 (2007).

[50] M. Mlejnek, E. M. Wright, and J. V. Moloney, Opt. Lett. **23**, 382 (1998).

[51] A. Couairon, and L. Bergé, Phys. Plasmas **7**, 193 (2000).

[52] D. Novoa, H. Michinel, and D. Tommasini, Phys. Rev. Lett. **105**, 203904 (2010).

[53] A. Couairon, S. Tzortzakis, L. Bergé, M. Franco, B. Prade, and A. Mysyrowicz, J. Opt. Soc. Am. B **19**, 1117 (2002).

[54] G. Fibich, S. Eisenmann, B. Ilan, and A. Zigler, Opt. Lett. **29**, 1772 (2004).

[55] A. Dubietis, G. Tamošauskas, G. Fibich, and B. Ilan, Opt. Lett. **29**, 1126 (2004).

[56] M. Centurion, Y. Pu, M. Tsang, and D. Psaltis, Phys. Rev. A **71**, 063811 (2005).

[57] A. Houard, M. Franco, B. Prade, A. Durécu, L. Lombard, P. Bourdon, O. Vasseur, B. Fleury, C. Robert, V. Michau, A. Couairon, and A. Mysyrowicz, Phys. Rev. A **78**, 033804 (2008).

[58] G. Méchain, A. Couairon, M. Franco, B. Prade, and A. Mysyrowicz, Phys. Rev. Lett. **93**, 035003 (2004).

[59] W. Liu, S. A. Hosseini, Q. Luo, B. Ferland, S. L. Chin, O. G. Kosareva, N. A. Panov, and V. P. Kandidov, New J. Phys. **6**, 6 (2004).

[60] P. P. Kiran, S. Bagchi, S. R. Krishnan, C. L. Arnold, G. R. Kumar, and A. Couairon, Phys. Rev. A **82**, 013805 (2010).

[61] S. A. Hosseini, Q. Luo, B. Ferland, W. Liu, S. L. Chin, O. G. Kosareva, N. A. Panov, N. Aközbek, and V. P. Kandidov, Phys. Rev. A **70**, 033802 (2004).

[62] N. A. Panov, O. G. Kosareva, V. P. Kandidov, N. Aköbek, M. Scalora, and S. L. Chin, Quantum Electron. **37**, 1153 (2007).

[63] A. J. Lichtenberg and M. A. Lieberman, *Regular and Stochastic Motion* (Springer-Verlag, New York, 1983).

[64] E. Ott, *Chaos in Dynamical Systems* (Cambridge University Press, Cambridge, 1993).

[65] C. T. Zhou, C. H. Lai, and M. Y. Yu, Phys. Scr. **55**, 394 (1997); J. Maths. Phys. **38**, 5225 (1997); C. T. Zhou and X. T. He, Phys. Scr. **50**, 415 (1994).

[66] C. Sulem and P. L. Sulem, *The Nonliear Schrödinger Equation: Self-Focusing and Wave Collapse* (Springer, New York, 1999).

[67] P. A. Robinson, Rev. Mod. Phys. **69**, 507 (1997).

[68] G. Fibich and B. Ilan, Opt. Lett. **26**, 840 (2001).

[69] T. W. Huang, C. T. Zhou, and X. T. He, AIP Adv. **2**, 042190 (2012).

[70] C. T. Zhou, X. T. He, and S. G. Chen, Phys. Rev. A **46**, 2277 (1992).

[71] H. T. Moon, Phys. Rev. Lett. **64**, 412 (1990).

[72] V. E. Zakharov and A. B. Shabat, Zh. Eksp. Teor. Fiz. **61**, 118 (1971) [Sov. Phys. JETP **34**, 62 (1972)].

[73] R. K. Bullough and P. J. Caudrey, *Soliton* (Springer-Verlag, Berlin, 1980).

[74] T. B. Benjamin and J. E. Feir, J. Fluid Mech. **27**, 417 (1967).

[75] B. Qiao, C. H. Lai, C. T. Zhou, X. T. He, X. G. Wang, and M. Y. Yu, Phys. Plasmas **14**, 112301 (2007).

[76] T. Höuser, W. Scheid, and H. Hora, J. Opt. Soc. Am. B **5**, 2029 (1988).

[77] Y. Tan and J. M. Mao, Phys. Rev. E **57**, 381 (1998); J. Phys. A **33**, 9119 (2000).

[78] C. Ren and W. B. Mori, Phys. Plasmas **8**, 3118 (2001).

[79] J. J. Rasmussen and K. Rypdal, Phys. Scr. **33**, 481 (1986).

[80] D. W. McLaughlin, G. C. Papanicolaou, C. Sulem, and P. L. Sulem, Phys. Rev. A **34**, 1200 (1986).

[81] S. N. Vlasov, L. V. Piskunova, and V. I. Talanov, Zh. Eksp. Teor. Fiz. **95**, 1945 (1989) [Sov. Phys. JETP **68**, 1125 (1989)].

[82] N. N. Akhmediev, D. R. Heatley, G. I. Stegeman, and E. M. Wright, Phys. Rev. Lett. **65**, 1423 (1990).

[83] L. Bergé, Phys. Rev. E **62**, R3071 (2000).

[84] W. Liu, S. L. Chin, O. Kosareva, I. S. Golubtsov, and V. P. Kandidov, Opt. Commun. **225**, 193 (2003)

[85] L. Bergé, C. Gouédard, J. S. Eriksen, and H. Ward, Physica D **176**, 181 (2003).

[86] C. T. Zhou, M. Y. Yu, and X. T. He, Phys. Rev. E **73**, 026209 (2006).

[87] C. T. Zhou, L. Y. Chew, and X. T. He, Appl. Phys. Lett. **97**, 051502 (2010); C. T. Zhou, X. G. Wang, S. Z. Wu, H. B. Cai, F. Wang, and X. T. He, *ibid*. **97**, 201502 (2010); C. T. Zhou, X. G. Wang, and X. T. He, Phys. Plasmas **17**, 083103 (2010).

[88] P. Béjot, B. Kibler, E. Hertz, B. Lavorel, and O. Faucher, Phys. Rev. A **83**, 013830 (2011).

[89] J. Kasparian, R. Sauerbrey, and S. L. Chin, Appl. Phys. B **71**, 877 (2000).

[90] A. Becker, N. Aközbek, K. Vijayalakshmi, C. M. Bowden, and S. L. Chin, Appl. Phys. B **73**, 287 (2001).

[91] W. Liu, S. Petit, A. Becker, N. Aközbek, C. M. Bowden, and S. L. Chin, Opt. Commun. **202**, 189 (2002).

[92] F. Théberge, W. W. Liu, P. Tr. Simard, A. Becker, and S. L. Chin, Phys. Rev. E **74**, 036406 (2006).

[93] M. B. Gaarde and A. Couairon, Phys. Rev. Lett. **103**, 043901 (2009).

[94] D. S. Steingrube, E. Schulz, T. Binhammer, M. B. Gaarde, A. Couairon, U. Morgner and M. Kovačev, New. J. Phys. **13**, 043022 (2011).

[95] P. P. Kiran, S. Bagchi, C. L. Arnold, S. R. Krishnan, G. R. Kumar, and A. Couairon, Opt. Express **18**, 21504 (2010).

[96] K. D. Moll, A. L. Gaeta, and G. Fibich, Phys. Rev. Lett. **90**, 203902 (2003).

[97] T. D. Grow, A. A. Ishaaya, L. T. Vuong, A. L. Gaeta, N. Gavish, and G. Fibich, Opt. Express **14**, 5468 (2006).

[98] S. L. Chin, N. Aközbek, A. Proulx, S. Petit, and C. M. Bowden, Opt. Commun. **188**, 181 (2001).

[99] S. L. Chin, S. Petit, W. Liu, A. Iwasaki, M. C. Nadeau, V. P. Kandidov, O. G. Kosareva, and K. Y. Andrianov, Opt. Commun. **210**, 329 (2002).

[100] K. Konno and H. Suzuki, Phys. Scr. **20**, 382 (1979).

[101] S. Tzortzakis, L. Bergé, A. Couairon, M. Franco, B. Prade, and A. Mysyrowicz, Phys. Rev. Lett. **86**, 5470 (2001).

[102] G. Méchain, A. Couairon, Y.-B. André, C. D'Amico, M. Franco, F. B. Prade, S. Tzortzakis, A. Mysyrowicz, and R. Sauerbrey, Appl. Phys. B **79**, 379 (2004)

[103] A. Pukhov and J. Meyer-ter-Vehn, Phys. Rev. Lett. **76**, 3975 (1996).

[104] Y. Y. Ma, X. Lu, T. T. Xi, Q. H. Gong, and J. Zhang, Appl. Phys. B **93**, 463 (2008).

[105] M. Segev, Opt. Quantum Electron. **30**, 503 (1998).

[106] Y. H. Liu, L. Y. Chew, and M. Y. Yu, Phys. Rev. E **78**, 066405 (2008).